DEVELOPMENT OF HYBRID PLASMONICS AND METAL OXIDE NANOSTRUCTURE CHIPS FOR VOCS OPTICAL SENSING DEVICE

KIRATIKARN CHANGPRADUB

A THESIS SUBMITTED IN PARTIAL FULFILLMENT OF THE REQUIREMENTS
FOR THE DEGREE OF MASTER OF ENGINEERING IN
MATERIALS ENGINEERING
DEPARTMENT OF MATERIALS AND PRODUCTION TECHNOLOGY
ENGINEERING
GRADUATE COLLEGE
KING MONGKUT'S UNIVERSITY OF TECHNOLOGY NORTH BANGKOK
ACADEMIC YEAR 2024

DEVELOPMENT OF HYBRID PLASMONICS AND METAL OXIDE NANOSTRUCTURE CHIPS FOR VOCS OPTICAL SENSING DEVICE

KIRATIKARN CHANGPRADUB

A THESIS SUBMITTED IN PARTIAL FULFILLMENT OF THE REQUIREMENTS
FOR THE DEGREE OF MASTER OF ENGINEERING IN MATERIALS ENGINEERING
DEPARTMENT OF MATERIALS AND PRODUCTION TECHNOLOGY ENGINEERING
GRADUATE COLLEGE
KING MONGKUT'S UNIVERSITY OF TECHNOLOGY NORTH BANGKOK
ACADEMIC YEAR 2024

Thesis Proposal Certificate

The Graduate College, King Mongkut's University of Technology North Bangkok

Title Development of hybrid plasmonics and metal oxide nanostructure chips for VOCs optical sensing device

By KIRATIKARN CHANGPRADUB

Accepted by the FACULTY OF ENGINEERING, King Mongkut's University of Technology North Bangkok in Partial Fulfillment of the Requirements for the Master of Engineering in Materials and Production Technology Engineering

..... Dean / Head of Department

(Assistant Professor SUPHOT CHUNWIPHAT)

Thesis Examination Committee

..... Chairperson

(Tossaporn Lertvanithphol)

..... Advisor

(Assistant Professor THOTSAPHON THRERUJIRAPAPONG)

..... Co-Advisor

(Mati Horprathum)

..... Committee

(Assistant Professor RUNGSINEE CANYOOK)

Name : KIRATIKARN CHANGPRADUB
Thesis Title : Development of hybrid plasmonics and metal oxide nanostructure chips for VOCs optical sensing device
Major Field : Materials Engineering
King Mongkut's University of Technology North Bangkok
Thesis Advisor :Assistant Professor THOTSAPHON THRERUJIRAPAPONG :
Co-Advisor : Mati Horprathum
Academic Year : 2024

ABSTRACT

In this study, a Localized surface plasmon resonance (LSPR)- based sensor for volatile organic compounds (VOCs) detection is developed. The sensors are fabricated as a hybrid nanostructure of gold nanoparticles (Au NPs) coated with a tantalum oxide (TaO) and Tungsten oxide (WO_3) thin film on a glass slide substrate through magnetron sputtering and thermal solid-state dewetting techniques. The thickness of the TaO and WO_3 film varies between 10 and 70 nm. The optical properties of samples are characterized by UV-Vis-NIR spectrophotometry, while their morphologies are confirmed via transmission electron microscopy. The results show the shift of the minimum optical transmittance related to the TaO and WO_3 thickness. Electrical field simulations are performed to predict the sensitivity of the prepared samples for VOC detection. In addition, the sensors are tested with different VOCs, including formaldehyde, isopropanol, acetone, methanol and Toluene which show good potential for practical applications.

Keywords Plasmonic, Au NPs, TaO, WO_3, Sputtering, VOCs, LSPR
:

_____ Advisor

ACKNOWLEDGEMENTS

Acknowledgement:

I would like to express my deepest and sincere gratitude to my advisor, Assistant Professor Dr. Thotsaphon Threrujirapapong whose expertise, patience, and encouragement guided me throughout this thesis work. I also extend my appreciation to my co-advisor Dr. Mati Horprathum for his inspiration and tremendous efforts in guiding and explaining concepts to me with clarity. I am profoundly grateful for the opportunity they provided me to work at the National Electronics and Computer Technology Center. I extend my warmest thanks to Dr. Tossaporn Lertvanithphol who offered his time, knowledge, and support throughout the research process.

My heartfelt appreciation also goes to my teachers, friends, and the staff of the Department of Materials and Production Technology Engineering for their continuous support. Additionally, I would like to acknowledge research funded by King Mongkut's University of Technology North Bangkok and National Science and Technology Development Agency, Thailand contract no. grad.012/2565 which was instrumental in facilitating my studies.

Finally, I wish to express my deepest gratitude to my parents, Teerachai and Nitsaya Changpradub, for their unwavering support and boundless love. Their encouragement has been integral to my journey, and without it, completing this thesis would not have been possible.

KIRATIKARN CHANGPRADUB

TABLE OF CONTENTS

Page

LIST OF TABLES

Table **Page**

LIST OF FIGURES

Figure **Page**

LIST OF ABBREVIATIONS

VOCs	Volatile organic compounds
LSPR	Localized surface plasmon resonance
RI	Refractive index
SSD	Solid-state dewetting technique
mTorr	millitorr
sccm	Standard cubic centimeters per minute
rpm	revolutions per minute
nm	nanometer
V/m	volt per meter
eV	electron volt
Pa	pascal
$\mu g/m^3$	microgram per cubic meter
mg/m^3	milligram per cubic meter
ppm	parts per million

CHAPTER 1
INTRODUCTION

1.1 Statement of the Problems

Volatile organic compounds (VOCs) constitute a diverse class of chemicals with boiling points ranging from 50-100 °C to 240-260 °C and molecular weights spanning from 50-70 to approximately 300 daltons[1]. These compounds are frequently used as ingredients in household products or industrial processes, where they vaporize at room temperature and can be inhaled. Unfortunately, many VOCs are known to have adverse health effects[2], [3]. Hence, the VOCs detection in environment is very important. While traditional analytical methods like gas chromatography-mass spectroscopy (GC-MS) offer accuracy and reliability[4]. However, this method was laboratory-based, highly skilled operators, time-consuming, and expensive, which are not applicable for point-of-use or real time detection[5], [6]. Consequently, the development of VOCs sensor platform has focused on cost-effectiveness, easy-to-use, portable size, and high sensitivity[7]. Several types of sensors for measuring volatile organic compounds in electric and optical platforms have been conducted in different aspects[8]. Nowadays, the electrical VOCS sensor platforms such as metal-oxide-semiconductor (MOS-type) sensors[9]and electrochemical sensors[10]are considered the best compromise in terms of technology maturity, sensitivity, cost, and device miniaturization potential. However, the performance of MOS-type sensors requires high operating temperatures (typically 150–500 °C) and poor gas selectivity. In the case of electrochemical sensors, they are limited by their low sensitivity in complex molecules and low stability[11]. The optical VOCs sensor platform presents numerous advantages, including low electromagnetic interference, low power consumption, room-temperature operation, and simplified sensor geometry, making fabrication straightforward[12]. In this context, the optical platform based on guided mode resonance (GMR) stands out as a notable option[13]. A distinctive characteristic of this sensor is its utilization of a thin film grating layer with a nanoscale pattern, and thin film waveguides that effectively trap light (optical waveguide). This configuration enables real-time monitoring and multiplexed detection of multiple VOCs. However, the challenge lies in the complex design required for producing nano-level patterns, which can only be achieved in a limited area. To avoid these problems, the VOCs detection based on localized surface plasmon resonance (LSPR) was represented. Which have recently emerged as a competitive technology platform with high sensitivity, fast response, and significant miniaturization potential. The phenomenon of localized surface plasmon resonance (LSPR)[14], which results from the plasmonic response of nanoparticles by incident electromagnetic waves, can be applied in the sensing of analytes. The mechanism is based on detecting the change in the environmental refractive index (RI). Recently, I. Tanyeli et al.[15]proposed a hybrid structure of nanoplasmonics combined with a metal oxide thin film. This hybrid structure can detect NO_2 gas in the air by changing the plasmonic signal in the presence of NO_2 gas.

Herein, we report on the fabrication of LSPR-based VOCs optical sensor chips. These chips consist of Au nanodots coated with the ultra-thin TaO and WO_3 film, fabricated through magnetron sputtering and solid-state dewetting methods. Notably, these fabrication processes enable mass production with lithography-free techniques, offering simplicity and cost-effectiveness. The effect of film thickness of the TaO and WO_3 layer from 10-70 nm was investigated. As a proof of concept, the VOCs sensing performance of our prepared chips was evaluated for detecting formaldehyde, isopropanol, acetone, methanol and Toluene. Our results demonstrated that the chip coated with an optimized TaO and WO_3 film thickness exhibited highly sensitive and selective responses to VOCs vapor.

1.2 Objectives

1.2.1 To study and develop hybrid plasmonic nanostructure of gold nanodots coated metal oxide thin film using DC magnetron sputtering and solid-state dewetting techniques.

1.2.2 To study parameters on the fabrication of nanostructures plasmonic layer and metal oxide thin film.

1.2.3 To characterize the physical and optical properties of the plaasmonics nanostructure and metal oxide thin film sensor.

1.2.4 To study VOC gas sensing of hybrid plasmonics nanostructure and metal oxide (MO) thin film sensor.

1.3 Scope of Study

1.3.1 Fabricate hybrid plasmonics nanostructure of gold nanodots coated tantalum oxide thin film at various thickness using DC magnetron sputtering and solid-state dewetting techniques.

1.3.2 Fabricate hybrid plasmonics nanostructure of gold nanodots coated tungsten oxide thin film at various thickness using DC magnetron sputtering and solid-state dewetting techniques.

1.3.3 Characterize the morphologies and optical characteristics of fabricated hybrid plasmonics nanostructure.

1.3.4 VOCs sensitivity and response test with fabricated hybrid plasmonics nanostructure.

1.4 Expected outcome

1.4.1 VOCs optical sensor-based hybrid plasmonic nanostructure of gold nanodots coated metal oxide thin films.

1.4.2 Sensitivity and response database of hybrid plasmonic nanostructure related to the material and thickness of metal oxide thin film layer.

1.4.3 Knowledge of VOCs sensing mechanism through the fabricated hybrid plasmonic nanostructure of gold nanodots coated metal oxide thin films.

CHAPTER 2
LITERATURE REVIEW

2.1 Volatile Organic Compounds (VOCs) Gas sensor

Volatile organic compounds (VOCs) are high vapor pressure of carbon-based compounds at room temperature and pressure and constitute a diverse class of chemicals with boiling points ranging from 50- 100°C to 240-260°C. The molecular weight range is from 50-70 to about 300 dalton[1]. which are frequently used as ingredients in household products or industrial processes. They are easily inhaled in daily life and known to have adverse health effects. When the molecules of those substances change to gas, they evaporate into the surrounding atmosphere in large amounts. It is directly harmful to the environment and human health. This vapor, if accumulated in the body for a long time, can damage the central nervous system. and increase the risk of cancer[16]. Standard concentrations of VOCs are shown in TABLE 2-1.

TABLE 2-1 Average standard concentrations of volatile organic compounds[17]

Volatile Organic Compounds	VOCs concentration standards, Pollution Control Department (μg/m3)	Occupational Safety and Health Administration Permissible Exposure Limit (OSHA PEL) (mg/m3)	Immediately Dangerous to Life or Health Concentrations (IDLH) (ppm)
1,3-Butadiene	< 5.3	2.21	2,000
Benzene	< 7.6	3.19	500
Carbon	< 150	62.9	200
tetrachloride	< 57	240	500
Chloroform	< 210	86.8	2,300
Dichloromethane	< 48	202.5	50
1,2-	< 130	537	1,000
Dichloroethane			
Trichloroethylene			

In addition to VOCs found in industrial products, VOCs are produced by organisms, both plants and animals. It can also release vapor. especially plants or meat that have been processed into raw food. When those foods are processed, the food degradation process begins immediately. This depends on environmental factors such as temperature, humidity, oxygen, amount of microorganisms, light. Quality degradation and deterioration that occurs in food means that the quality of food changes in terms of color, aroma, taste, shape, appearance, texture, and nutritional value. as well as safety for consumption[18]. The main factor of food deterioration is caused by microorganisms each type of food has different chemical components such as

carbohydrates, proteins, fats, vitamins, minerals, resulting in different values of the acid-base or pH and amount of water that are appropriate for microbial growth vary depending on the type and quantity found. The shelf life of fresh food therefore varies. As shown in TABLE 2-2.

TABLE 2-2 Shelf life of various types of food at 21 degrees Celsius[19]

Type of foods	Shelf life (days)
Meat	1 – 2
Fruits	1 – 7
Vegetable	1 – 2
Tuber	7 – 20
Dried fruit	> 360

Foods that are high in protein, such as meat, seafood, milk, and nuts, deterioration is often caused by bacteria (proteolytic enzymes) such as protease, that breaks down large protein molecules (amino acids). Furthermore, decomposes them into Volatile substances that have a bad smell, such as the decomposition of amino acids that contain sulfur (sulfur) as a component, such as the amino acid (cystein) produce hydrogen sulfide gas (hydrogen sulfide, H_2S). which has an odor. Rotten eggs, the breakdown of the amino acid tryptophan produces indole and skatole, which have a putrid odor similar to feces or in the case of foods that are high in fat Microorganisms that have lipolytic enzymes, such as lipase, will digest triglycerides. (triglyceride) into a free fatty acid molecule (free fatty acid). If it is a short chain fatty acid, it evaporates easily and has an odor. Free fatty acids, which are unsaturated fatty acids, can also react with oxygen in the air (lipid oxidation) causing rancidity. Examples of reactants and products from spoilage by microorganisms Shown in TABLE 2-3.

TABLE 2-3 Products of microbial decomposition[20]

Reactant	Substances produced by bacteria
TMAO	TMA
cysteine	H_2S
methionine	CH_3SH, $(CH_3)_2S$
carbohydrates and lactate	acetate, CO_2, H_2O
inosine, IMP	Hypoxanthine
amino acids (glycine, serine, leucine)	esters, ketones, aldehydes
amino acids, urea	NH_3

2.2 Localized surface plasmon resonance (LSPR)

Surface plasmon resonance (SPR) is a phenomenon in which light interacts with electrons on the metal surface where the light hits. This causes plasmon which results from free electrons on the metal surface vibrating perpendicular to the surface and propagating parallel to the metal surface. As shown in FIGURE 2-1, when the frequency of light incident on a metal surface is equal to the natural frequency of free electrons, it causes resonance or resonance, causing the incident light to be absorbed. Can absorption and convert to plasmon the highest[21-24]

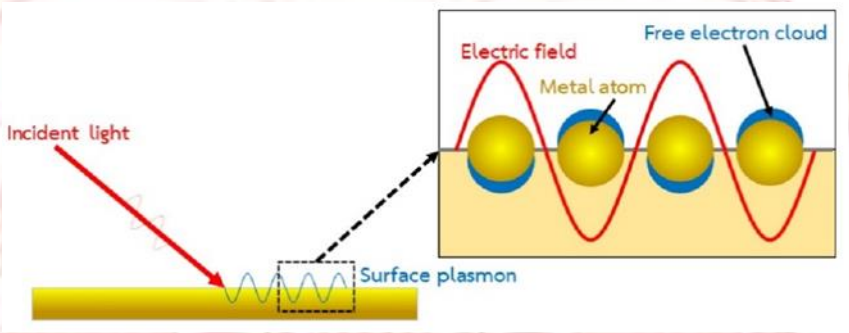

FIGURE 2-1 Surface and propagating parallel to the metal surface

Although measurement techniques based on the surface plasmon resonance phenomenon of gold thin films can measure specific biomolecules, however, the plasmon field generated by the SPR phenomenon will affect the surface of the gold thin film over 250 to 1,000 nm, as shown in FIGURE 2-2. However, in measuring surface changes such as the adhesion of molecules on the surface. The field of plasmons is too high from the surface. It easily causes interference from the surrounding environment. To solve this problem Localized surface plasmon resonance (LSPR) is a phenomenon that occurs when light hits nanoscale structures. Plasmonic nanostructures have therefore been developed to measure surface changes that require high responsiveness. This is because the resulting plasmon field affects only 20 to 40 nanometers from the surface of the nanostructure, as shown in FIGURE 2-2 [21-22], [25].

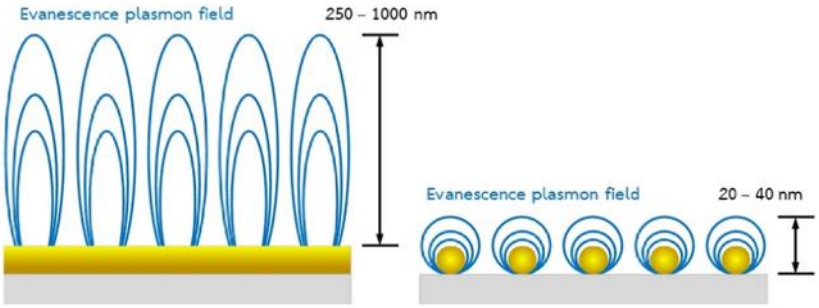

FIGURE 2-2 Plasmon field generated by the SPR and LSPR phenomenon

To measure surface changes using the LSPR phenomenon, the optical transmission signal of plasmonic nanostructures is measured, which has a unique pattern. The optical transmittance is lowest at specific wavelengths. As shown in FIGURE 2.3, this wavelength is called Resonance Wavelength. When molecules adhere to the surface of the plasmonic nanostructure, or within a range where the plasmon field from the LSPR phenomenon still has an effect. The optical transmission signal changes as the resonance wavelength position shifts away from the original value[21], [25]. As shown in FIGURE 2.3.

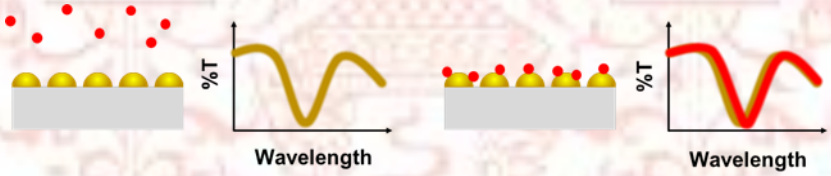

FIGURE 2-3 Schematic of optical transmission signal in LSPR phenomenon

2.2.1 Factors affecting the occurrence of LSPR phenomenon on Metal surfaces

From the literature review It was found that the type of metal has a direct effect on the absorption range of light that causes the LSPR phenomenon on the surface of the metal. Silver (Ag) and gold (Au) have a response to light in the range. visible light to near infrared (NIR)[26], while aluminum (Al) responds to light in the range of ultraviolet (UV) to visible light as shown in TABLE 2-4. The vast majority of LSPR sensing experiments have been carried out on gold or silver nanoparticles. Gold is often chosen because of its chemical stability and resistance to oxidation, but silver has sharper resonances and higher refractive index sensitivity. However, when considering its chemical stability (chemical stability) It was found that gold metal is the most stable when oxidized. As a result, gold metal is widely synthesized into nanoscale structures for the LSPR phenomenon[27].

TABLE 2-4 Plasmonic properties and chemical stability of various metals[27]

Metals	Plasmonic Characteristics			Chemical stability
	Ultraviolet	Visible light	Near-infrared	
Silver (Ag)	-	✓	✓	Easily oxidized
Gold (Au)	-	✓	✓	Stable
Aluminum (Al)	✓	✓	-	Easily oxidized

2.3 Sputtering Mechanism

The techniques used for the Tantalum oxide (TaO) and Tungsten Trioxide (WO_3) thin film deposition purposes could be broadly classified as Physical Vapor Deposition (PVD) and Chemical Vapor Deposition (CVD) processes. In this research, Tantalum oxide (TaO) and Tungsten Trioxide (WO_3) thin film are decorated by the sputtering method. Notably, these fabrication processes enable mass production with lithography-free techniques, offering simplicity and cost-effectiveness. Sputtering, one of the most important techniques of PVD processes employs momentum transfer between the impacting ion and target. The ion bombardment causes an atom-by-atom ejection of the target material that can then condense and deposit on the substrate place opposite the target. As shown in Figure, when an ion approaches the surface of a solid (target) one or all the following phenomena may occur[28].

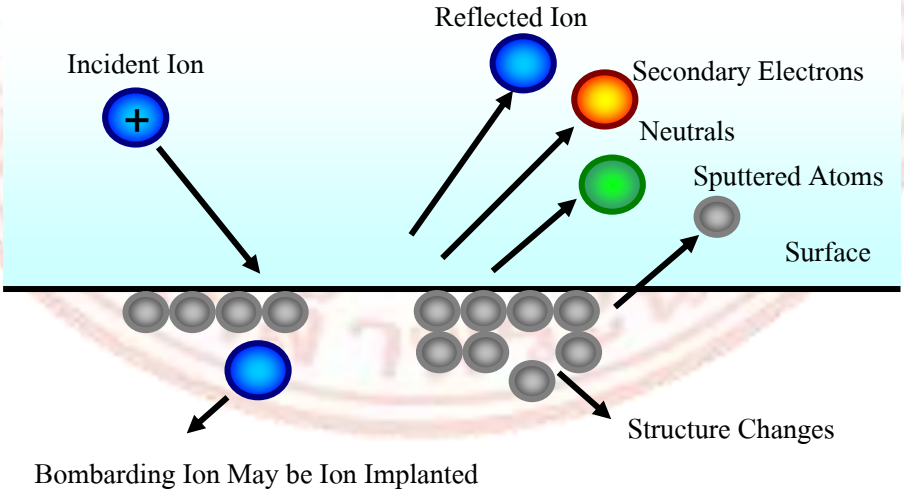

FIGURE 2-4 The Interactions of ions with surfaces[28].

a) The ion may be reflected, probably being neutralized in the process.

b) The impact of the ion may cause the target to eject an electron, usually referred to as a secondary electron.

c) The ion may become buried in the target. This is the phenomenon of ion implantation.

d) The ion impact may also be responsible for some structural rearrangements in the target material.

e) The ion impact may set up a series of collisions between atoms of the target, possibly leading to the ejection of one of these atoms. This ejection process is known as sputtering.

When an ion with energy of more than 30 eV hits a surface, a small fraction of the energy and momentum of the incoming ion will, through lattice collisions, be reversed and may cause ejection of surface atoms, i.e. sputtering[29]. The sputtered atoms leave the target surface with relatively high energies (~10 eV) compared with evaporation atoms (~0.1 eV). The average number of atoms ejected from the surface per incident ion is called the sputtering yield[29]. The ion source is usually plasma (i.e., an electrically neutral mixture of positive ions and electrons) generated by electron impact in a noble gas at subatmospheric pressures (typically 2 - 10 Pa). The ions are accelerated in an electric field obtained by applying a negative potential with respect to the plasma potential to an electrode immersed in that plasma. The ejected or sputtered atoms can be condensed on a substrate to form a thin film. The sputtering yield (S) depends on many factors, such as the mass and the energy of the incident particles, the mass and the binding energy of the sputtered atoms, the crystallinity of the target, etc., and can be described as[30], [31]:

$$S = \text{const}\,(E_{ion} - E_{thres}) = \text{const}\, e(V_p - V_{dc} - V_{thres}), \quad (2\text{-}1)$$

$$E_{thres} = 8U_s(M_1/M_2)^{2/5} \quad (2\text{-}2)$$

Where:

E_{ion} is the energy of the incident ion

E_{thres} is a threshold energy

V_p is the plasma potential

V_{dc} is the dc voltage on the target (discharge voltage)

U_s is the surface potential barrier and M_1 and M_2 are the mass number of the ion and the target. The deposition rate R is proportional to the sputtering yield S, and $I(1 - \gamma)$, with I the discharge current and γ the secondary electron emission coefficient[32]

$$R = \text{const } SI(1-\gamma) \tag{2-3}$$

2.3.1 DC Sputter Deposition[28-29], [33]

The momentum transfer process that accompanies the bombardment of a surface by a high-energy ion can result in the physical sputtering of a surface atom. This sputtered surface, called a “sputtering target”, is the vaporization source for the sputter deposition. In plasma-based sputtering, ions are formed in plasma and accelerated to the surface under an applied potential. The simplest of these plasma configurations is DC sputtering, where a high DC voltage is applied to a conductive surface in a gas, plasma is formed near the surface, and ions are accelerated to the surface, as shown in FIGURE 2-5. In the DC glow discharge, the electric field strength is high near the cathode and most of applied voltage is “dropped” across a region near the surface, call cathode dark space. The cathode dark space region is very important to sustain the discharge as well as the sputtering process. The large voltage drop that occurs across dark space is responsible for the acceleration of ions that enter the dark space by diffusion from the negative glow region. These ions impact upon the cathode with considerable energy to give rise to the sputtering process. The ions also are neutralized by the impact of the cathode and give rise to the liberation of electrons from the cathode. These latter electrons are accelerated away from the cathode by the dark space field and quickly gain enough energy to engage in ionizing collisions with neutral argon gas atoms. For the discharge to be self-sustaining, each argon ion that is neutralized at the cathode must be replaced by another argon ion generated by ionizing collision caused by a liberate electron. Otherwise, the cathode would drain ions from the negative glow region. Neutralize these, and the discharge would quickly be extinguished. This latter condition can occur if the anode is brought very close to the cathode surface, and electron reach the anode before causing a sufficient number of ionizing collisions. The anode spacing needed to accomplish such discharge extinction is the dark space distance. Therefore, to prevent a discharge from forming near some portions of the cathode surface, the placement of an anode at the distance less the dark space length it required.

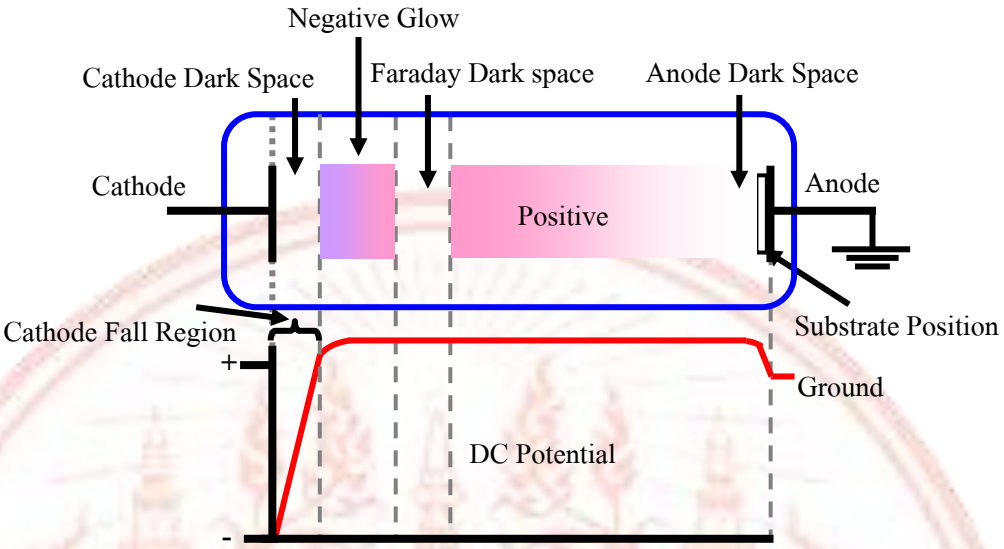

FIGURE 2-5 DC discharges showing the potential distribution between the electrodes and the behavior of the electrons and ion in the cathode dark-space region[28]

The dark space length is a function of pressure as well as the nature of the gas. As the pressure is reduced, the dark space length becomes equal to anode cathode spacing, and discharge extinguish. This even limits the practical utilization of DC diode sputtering to pressure of the order of 40 mTorr. However, if these electrons were better utilized, the pressure at which dc sputtering occurs would be reduced. Suitably oriented magnetic field accomplishes this by causing the electrons to move in spiraling paths, thereby substantially increasing the electron path in traveling from cathode to the anode. As might be expected, the use of such magnetic fields caused the dark space length to decrease. Typical dark space lengths encountered in DC diode sputtering range from 1-2 cm, whereas in some magnetically enhanced dc magnetron method, as will be discussed in section 2.3.2, the dark space length is reduced to 0.5 mm. The mean free part of electrons is a function of gas density n (atoms/cm^3) and the effective collision cross-section (α)

$$L = 1/n\alpha \qquad (2\text{-}4)$$

The cross section for ionizing type collisions between an electron and inert gas is a function of electron velocity. The atom will appear large to slowly moving electrons, and small to rapidly moving electrons. Thus, the event in the dark space

can now be visualized as follows: some electrons, purely by change suffer an ionizing collision an argon atom very early in their travels through the dark space. These electrons are slowed and create another slow electron. The mean free path remains short because these electrons are moving slowly. Other electrons, again purely by chance, travel a long distance through dark space, and thereby gain large amounts of energy from the dark space field. These electrons now do not suffer any ionizing collisions because of their long mean free part, the bombard the substrate with the full energy gained by traversing the dark space field. These high-energy secondary electrons are the single most important source of substrate heating encountered in DC sputtering.

2.3.2 Magnetron Sputtering Deposition [28-29], [33-34]

Magnetrons sputtering devices have become popular from easiness in technical adjustment and film quality. Magnetrons have been more routinely used to rapidly deposit thin metal films for a broad range of applications from architectural glass and food packaging to thin films microelectronics. The DC diode sputtering configuration is not widely used because of its poor sputtering efficiency. This is because the secondary electrons that are accelerated away from the cathode are not effective in producing ionization, and the high gas pressure necessary to sustain the discharge prevent ions from attaining high energies before they strike the sputtering target. Compared to the DC diode sputtering process shown in FIGURE 2-6 (a), the planar target in its simplest form is shown schematically in FIGURE 2-6 (b). It consists of the target material backed by permanent magnets that provide a toroidal confinement field with the field lines forming a closed tunnel on the target surface. The field strength is chosen to provide effective confinement for electrons while allowing heavier ions considerable freedom.

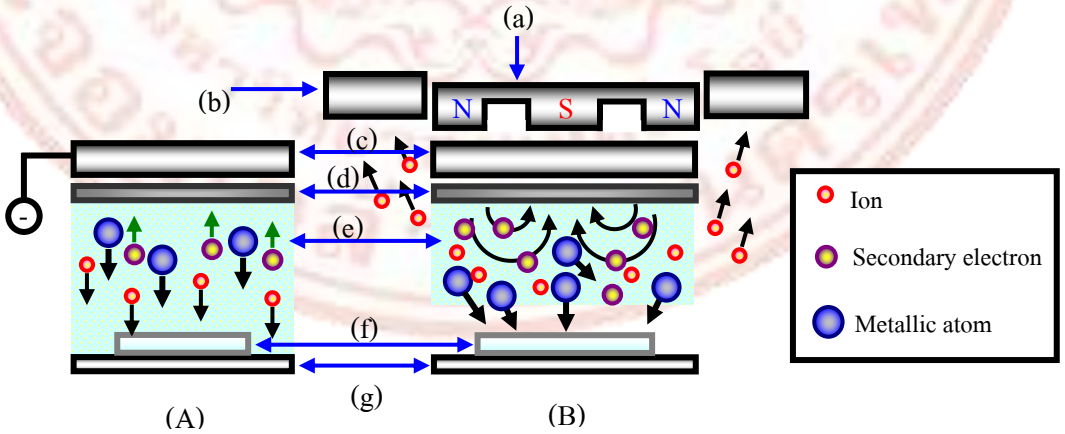

FIGURE 2-6 Schematic illustrations of the (A) convention dc-diode and (B) planar magnetron cathode sputtering (a. magnet field line, b. the wall of vacuum chamber, c. cathode, d. target, e. plasma, f. substrate, g. anode)[29].

Magnetrons are a class of cold cathode discharge devices used generally in a diode mode. The plasma is initiated between the cathode and the anode at pressures in the mTorr range by the application of a high voltage that can be either DC or RF. The plasma is sustained by the ionization caused by secondary electrons emitted from the cathode due to ion bombardment which are accelerated into the plasma across the cathode sheath. What differentiates a magnetron cathode from a conventional diode cathode is the presence of a magnetic field. The magnetic field in the magnetron is oriented parallel to the cathode surface. The local polarity of magnetic field is oriented such that E×B drift of the emitted secondary electrons forms a closed loop. Due to the increased confinement of the secondary electrons in this E×B drift loop compared to a DC or RF diode device, the plasma density will be much higher, often by an order of magnitude or more, than a conventional RF or DC diode system. The result of the high plasma density and its proximity to the cathode is a high current, relatively low voltage discharge. Typical discharge parameters for a magnetron might be a voltage of 500 V and a current of 5 A, whereas a non-magnetized diode might operate at 2500 V and 0.5 A. Due to the effective trapping of the energetic secondaries close to the cathode, a high plasma density can be sustained at significantly lower chamber pressures than similar power RF or DC diode plasma. A magnetron operates at a pressure ranging from 1-2 mTorr to 30-40 mTorr, whereas a typical RF diode might operate at 15-200 mTorr. The low operating pressure results in a significant reduction in gas scattering between the sputtered atoms and the background gas. The result of this reduction is an effective increase in the average kinetic energy of the sputtered atom (less thermalization) and an increase in the probability of atom transport from the cathode to the substrate. The result of the high discharge currents is the ability to sputter the cathode at a high rate. The deposition rate on surfaces within 5-10 cm from the cathode may be as high as several microns/minute for high sputter yield materials. Usually, the typical limiting factor to the maximum deposition rate in a magnetron device is the ability to cool the cathode. Magnetrons have been developed in a wide range of geometries: each of which satisfies the requirement that the E×B drift path forms a closed loop. Three basic classes of geometries exist: the planar, the cylindrical and the conical designs. The planar design (FIGURE 2-7(a)) is available in a circular geometry at diameters of from 5 to a few 10’s of cm. The rectangular or “racetrack” magnetron (FIGURE 2-7(b)) has been developed at lengths exceeding the meter range. Cylindrical geometry is characterized by a central, cylindrical cathode with an axial magnetic field (FIGURE 2-7(c)). The magnetic field in this case is radial and the resultant E×B drift path forms a band around the cathode. The third geometry is the conical design (FIGURE 2-7(d)), which is somewhat similar to the circular planar device.

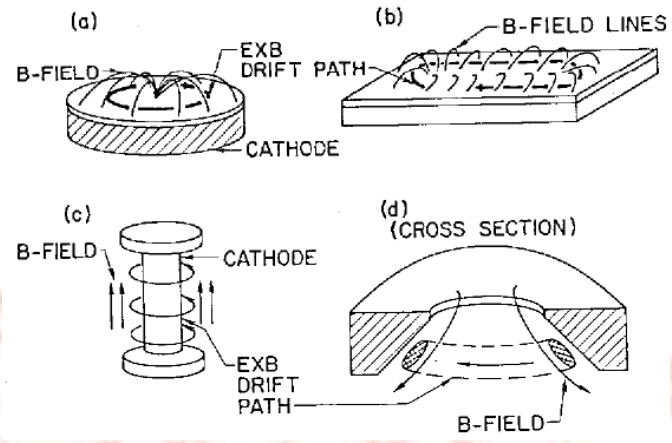

FIGURE 2-7 (a) Circular planar magnetron, (b) rectangular planar magnetron, (c) cylindrical posy magnetron and (d) conical magnetron[28]

2.3.3 Reactive Sputtering[30]

Reactive sputtering is the method in which thin films of compounds are deposited on substrates by sputtering from metallic targets using both the inert working gas and a reactive gas. The dynamics of this process as a function of reactive gas flow is depicted in FIGURE 2-8. At low flow rates all the reactive gas is incorporated into the deposited film (metallic mode). As the gas flow rate is increased, a threshold is reached where the target surface experiences compound formation. When this compound formation exceeds the removal rate of material, a threshold is reached that is accompanied by a sharp decrease in sputtering rate and discharge voltage (compound mode). This decrease is due to the fact that compounds generally have lower sputtering rates and higher secondary electron emissions. Additionally, a third cause for the drop in sputtering rate is due to less efficient sputtering by reactive gas ions than by inert ions. When the reactive gas flow is sufficiently reduced the system will revert to metallic mode. However, metallic mode sputtering will not commence at the same flow rate, because the compounds remaining on the target need to be removed before normal sputtering can resume.

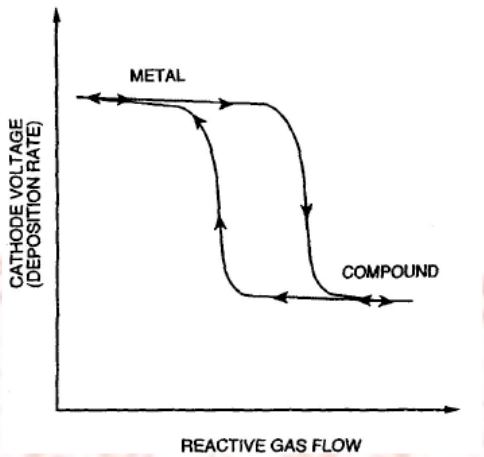

FIGURE 2-8 Generic hysteresis curve for voltage vs. reactive gas flow rate[30].

2.4 Nucleation and Growth of thin film

The nucleation and growth process of thin film begins as sputtered particles arrive at the substrate surface and become physically absorbed. Initially these particles are not in thermal equilibrium with the substrate, so it move and interacts with other particles. The mobility of atoms arriving at the substrate depends on the substrate temperature and the binding energy of atoms. Clusters of particles that form are not thermodynamically stable will be desorbed from the surface. Thermodynamically stable clusters have overcome the nucleation barrier and will begin to grow[35]

These nuclei grow across the surface of the substrate by atom surface diffusion until islands grow large enough to coalescence and begin to grow vertically by the arrival of sputtered species. The coalescence growth stage arises when these islands grow large enough to touch and continues until the film reaches continuity (Westwood, 1976). The islands start to coalesce to reduce the overall surface area of the growing film. This tendency to form larger islands is known as agglomeration. When the islands grow together, the film goes from a discontinuous islands type to a porous network type. This type of growth will continue until all islands have grown together and will a continuous film[35]. There are three nucleation and growth stages for deposition in FIGURE 2-9. Films grown by coalescence of islands are known as Volmer-Weber type[35]Volmer-Weber occurs when sputtered atoms are bound more tightly to each other than the substrate, such as in the growth of metal films on insulators.

Films that grow layer by layer are known as Frank-van der Merwe type. Frank-van der Merwe growth occurs when lattice mismatch is small and the binding energy of sputtered atoms is equal to or less than the binding energy of sputtered atoms to the substrate. Those that grow by a mixture of the two are called StranskiKrastanov type[35]. A graphical summary of the initial growth stages as shown in FIGURE 2-10.

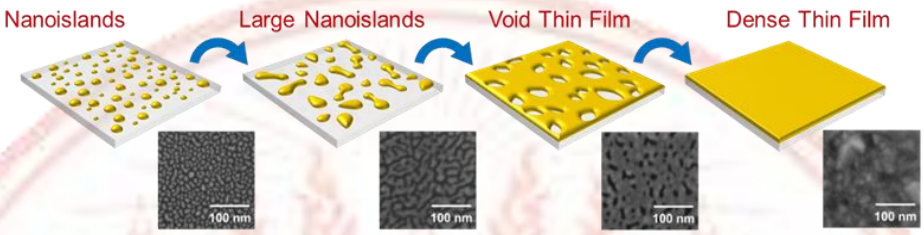

FIGURE 2-9 Basic of film growth process: (a) nucleation, vapor atom condense and bind together to create atomic-scale nuclei at random surface location, (b) island growth, (c) coalescence of islands together to form a void Thin film and (d) dense thin film.

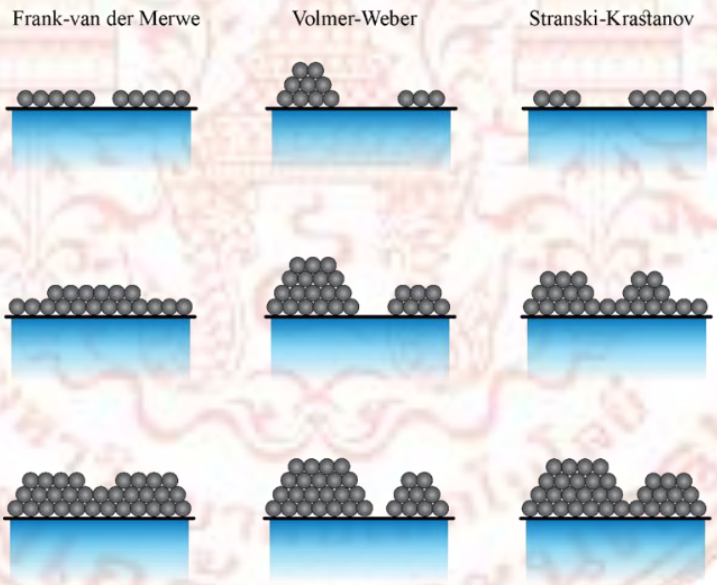

FIGURE 2-10 Basic modes of thin-film growth mechanism[36].

(a) Layer (or Frank-van der Merwe)

(b) Island (or Volmer-Weber)

(c) Stranski-Krastanov

2.5 Structure Zone Model [30], [35], [37-42]

Films prepared by physical vapor deposition show a wide range of microstructures and properties, both of which are highly dependent on the preparation conditions. In case of sputter deposition, which is the method of interest in this work, the transport of the atoms to the substrate is controlled by parameter such as the apparatus geometry and working gas pressure, while diffusion steps are controlled largely by the substrate temperature but may be significantly influenced by energetic particle bombardment. Various models describe the influence of the deposition parameters on the structure of thin films. The microstructure and morphology of thick evaporated coating have been extensively studied by Movchan and Demchishin(1969). They concluded that the coatings could be represented as a function of T/T_m in terms of three zones, each with its own characteristic structure and physical properties. Thornton (1975) extended this model to sputtering by adding an additional axis to account for the effect of the sputtering gas. Messier [41](1984) revised the zone model by adding the effect of ion bombardment- and thermal-induced mobility when a bias to the substrate is applied. Later Kelly et al.[42]developed a structure zone model relating to the closed field unbalanced magnetron sputtering system, where coating structures are described in terms of homologous temperatures, bias voltage and ion-to-atom incident at the substrate. Barna and Adamik[43](1998) modified further the structure zone model constructed in conjunction with the concentration of impurities. By analyzing the structure zone models published in the literature, the various structure zones can be characterized by the following way FIGURE 2-11.

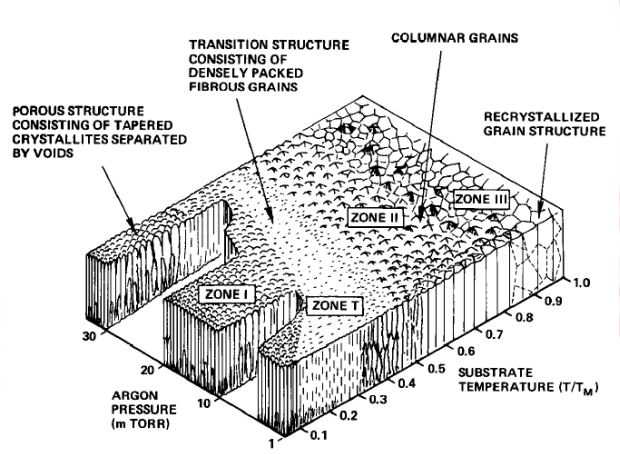

FIGURE 2-11 Schematic representation of the influence of substrate temperature and argon pressure on the microstructure of metal coatings deposited by cylindrical magnetron sputtering. The ratio of substrate T_s to film melting (T_s/T_m) increases in the direction Z1 → ZT → Z2 → Z3.[44]

In zone I, the film is composed of fibers of small diameters (1-10 nm) determined by the nucleation density and statistical fluctuation. The crystalline fibers grow out of the primary nuclei and proceed to the top of the film.

The fibers are often collected into bundles. This is a rather homogeneous structure along the thickness of the film with increasing diameter of fibers by increasing T_s/T_m. The crystals contain probably high density if defects and the grain boundaries are porous. This structure belongs to the temperature interval $0< T_s/T_m <0.2$ where neither the bulk diffusion nor the self-surface diffusion has a remarkable value.

In zone T, the structure is inhomogeneous along the film thickness. There are fine crystalline phases at the substrate, composed of V-shape grains in the next thickness range. The grains may become columnar in the upper part of thick films. This zone belongs generally to the temperature interval $0.2< T_s/T_m <0.4$ in which self-surface diffusion is remarkable but the grain boundary migration is strongly limited.

Zone 2 represents a homogeneous structure along the film thickness composed of columns penetrating from the bottom to the top of the film. The grain boundaries are nearly perpendicular to the film plane. This zone corresponds to the area of high substrate temperatures ($T_s/T_m >0.4$).

In zone 3, the structure is characterized by equiaxed (globular) three-dimension grains. This kind of structure is generally attributed to the high substrate temperature range.

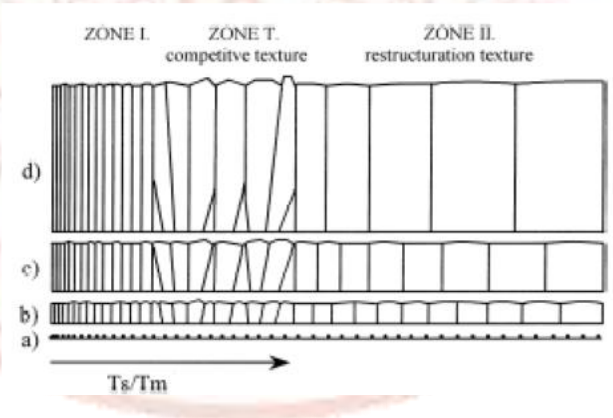

FIGURE 2-12 Basic structure zone with various thickness[30]

FIGURE 2-12 illustrates the structures at various temperatures with increasing film thickness. Nucleation density determines lateral sizes of the fibers in the temperature interval corresponding to Zone 1. The orientation of fibers follows the random orientation of the nuclei. The competitive growth of differently oriented neighboring crystals is developed in Zone T. The texture changes with the thickness in this zone. The near substrate part shows random orientation while the competitive growth texture is increasing as film grows. As the temperature increases, the effect of grain boundary migration increases. Randomly oriented small grains are dissolved gradually by coalescence and grain coarsening. This strong reconstruction is controlled by the minimization of the interface and surface energy and develops the reconstructive growth texture.

2.6 Solid-state dewetting Technique (SSD)

From the literature review it was found that in the film coating process using Physical Vapor Deposition (PVD) Techniques, including Sputtering techniques is widely used for Thin-film solid-state dewetting (SSD) for metallic nanostructures. in which the thin-film undergo void nucleation, film rupture, rim retraction and nanostructure formation[45], [46] as seen in FIGURE 2-13. As the process of nanostructure formation is relatively random, the low-developed nanostructures in early SSD stage can obtain wiggly shapes and thus lead to the various dielectric properties for individual nanostructures.

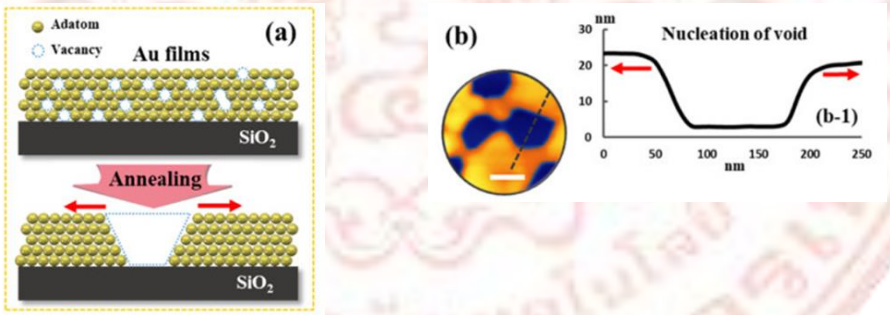

FIGURE 2-13 Diagrams of (a) Au film evolution (b) through solid-state-dewetting [47]

Used gold thin films as plasmonic chips, The gold thin film must have the appearance of nanodots with a size of approximately 100 nanometers, which is similar to the structure of the gold thin film prepared by the physical vapor deposition technique during the initial formation. It is an island nanostructure. However, the size of the island nanostructure is much smaller than 100 nanometers, making it impractical for practical use. Therefore, the idea was to take the porous thin film and anneal it with heat (Thermal annealing) close to the temperature at the melting point of the gold thin film. This causes the gold thin film to shrink around the cracks and causes them to

separate each separated gold mass shrinks and solidifies into a nanodot structure of gold material on the surface of the support plate as the temperature decreases[48], [49].

CHAPTER 3
RESERCH METHODOLOGY

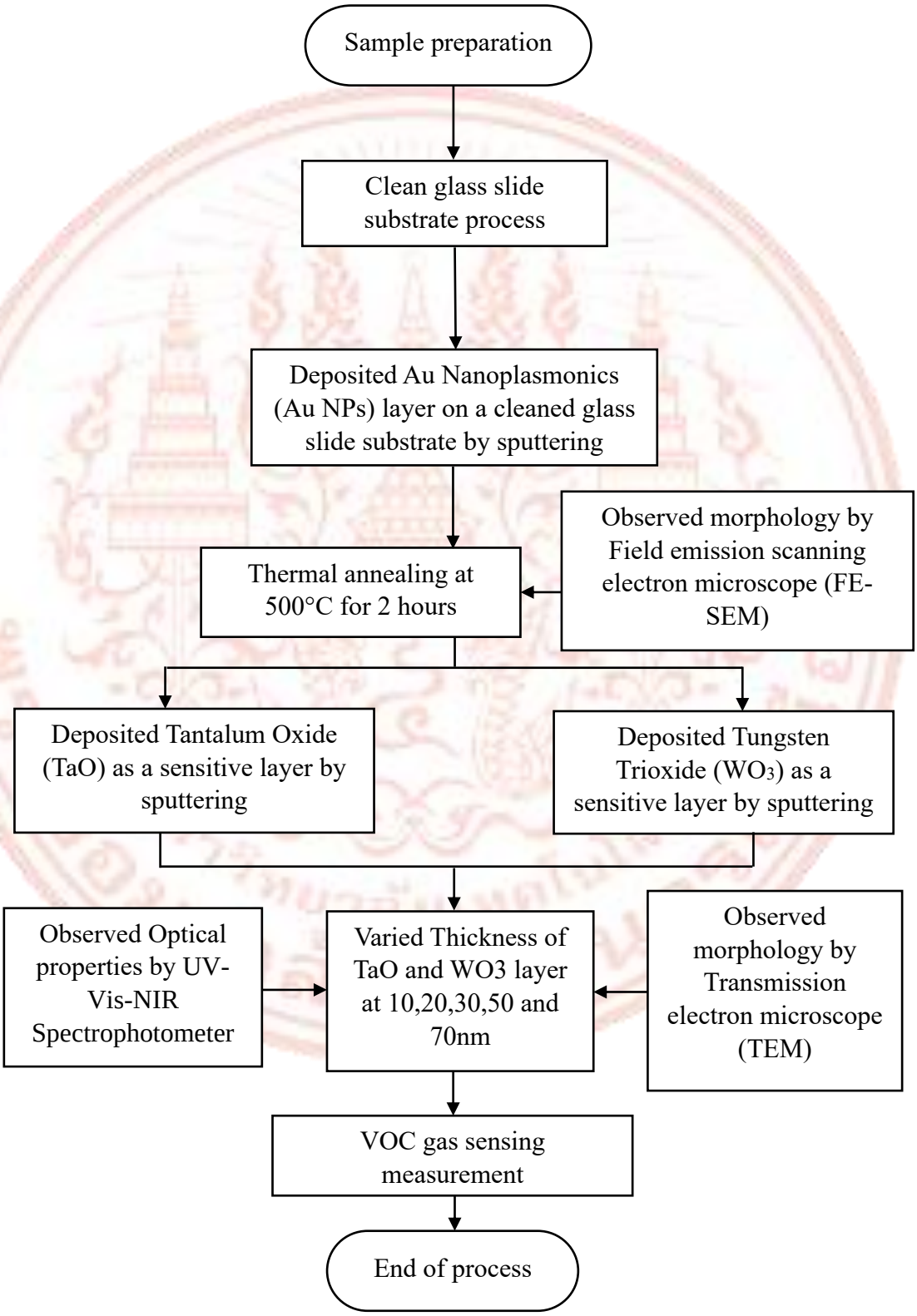

Instrumentation and Experimental

In this chapter the instruments and experimental methods used for the preparation and characterization of Hybrid plasmonic and metal oxide (TaO and WO_3) thin films. These films are prepared on glass slide substrates using a pulse DC reactive magnetron sputtering system with Au nanoplasmonics (Au NPs) and pure TaO, WO_3 metal targets. The characterization methods employed include Field Emission Scanning Electron Microscopy (FE-SEM), Transmission Electron Microscopy (TEM), UV-VIS-NIR spectrophotometry (UV-VIS), and VOCs optical measurement setup. Additionally, various instruments, electronic devices and chemical materials used for film preparation and characterization have been supported by multiple institutions.

3.1 Film Deposition Instruments and Substrate preparations

This research has been prepared by various institutions for instruments for substrate preparation and thin-film deposition.

3.1.1 Thin-film Deposition by Sputtering Systems

In this research, LSPR-based VOC optical sensors were fabricated on a glass slide substrate using a commercial magnetron sputtering system (AJA International, Inc. ATC 2000-F) at The Optical Thin Film Laboratory, National Electronics and Computer Technology Center (NECTEC), as shown in Figure 3-1 A High-Temperature Furnace (EF-6L), depicted in Figure 3-2, was also used. The sputtering system is equipped with DC, pulsed DC, and RF generator power supplies, delivering up to 500 watts of power and controlling the heating system up to 700 °C. The vacuum system comprises a mechanical rotary pump (ALCATEL) and a turbo-molecular pump (Shimadzu, TMP-803-LM). Samples were prepared in a turbo-pumped load lock chamber, reaching a base pressure lower than 10^{-7} Torr in both the main and load lock chambers. The equipment is supported by a cooling water system.

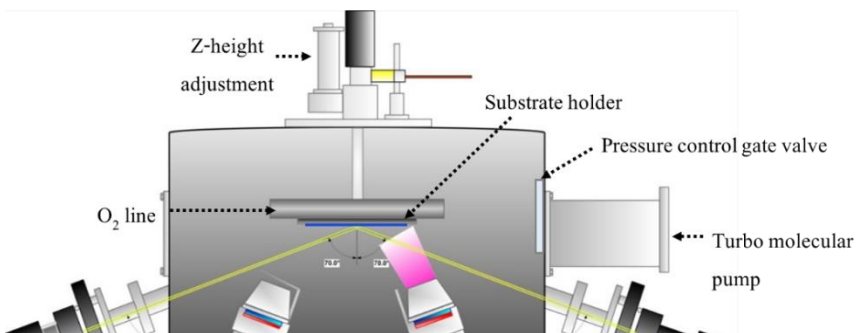

FIGURE 3 -1 (a) The schematic of DC, DC pulsed, and RF magnetron sputter deposition system (b) AJA International, Inc. (ATC 2000-F) at The Optical Thin Film Laboratory, National Electronics and Computer Technology Center (NECTEC)

3.1.2 Substrate and cleaning process

Concisely, to obtain a high-quality film, it is necessary to clean substrate thoroughly, a glass slide substrate, made in German. was sequentially cleaned in an ultrasonic bath are listed as the following:
(1) Rinsed and sonicated in deionized water
(2) Ultrasonic oscillation in Acetone for 10 min
(3) Ultrasonic oscillation in Isopropanol for 10 min
(4) Ultrasonic oscillation in Deionized water for 10 min
(5) Dry blowing with Nitrogen flow
(6) Plasma cleaning by Argon ion for 10 min

3.2 AuNPs Deposition

After the substrates were prepared by ultrasonic washer with Acetone, Isopropanol, Deionized water and dried with nitrogen flow, successively. And loaded it into the load lock chamber. When the pressure at the load lock chamber below 10^{-5} Torr, Then the substrates were into the main chamber. Prior to the Gold (Au) deposition, the substrate was cleaned by Argon plasma ion at 5 mTorr for 10 minutes to ensure a non-contaminated surface.

TABLE 3 -1 The deposition condition of AuNPs thin film

Deposition Parameters	
Substrate	Glass slide (25 × 25 × 1 mm)
Target	Au (99.5%)
Based Pressure	5×10^{-6} mTorr
Operating Pressure	5×10^{-3} mTorr
Ar Flow rate	20 sccm
O_2 Flow rate	7 sccm
Sputtering Power (DC-pulse)	100 Watt
Rotation Speed	20 rpm

The samples are annealed at a temperature of 500°C. The Au (99.5%) in the thin film will be annealed in Muffle Furnace (EF-6L). due to its high surface energy When gold melts, the surface energy decreases. At the same time, the liquid gold is pulled back into a small sphere (dot), resulting in the AuNPs nanodot structure. The Thermal annealing process is shown as follows
(1) Heated in a muffle furnace at 500°C for 2 hours
(2) Cooled at room temperature
Due to the sample must heated at range from room temperature (25°C) to 500°C, the temperature-time relationship is as shown in Figure 3-3.

FIGURE 3 -2 High-Temperature Furnace (EF-6L)

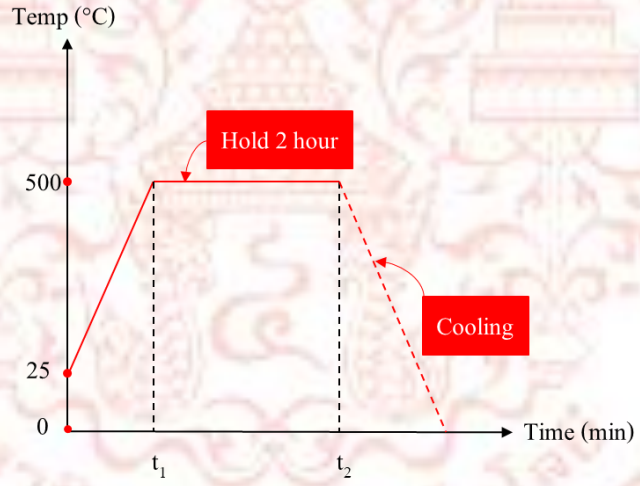

FIGURE 3 -3 Temperature-Time relationship

3.3 TaO and WO_3 Thin film deposition

After the sputtered Au samples were annealed at 500°C for 2 hours in ambient air and cooled naturally to room temperature (25°C). Next, the ultra-thin TaO and WO_3 thin films were deposited on an annealed Au sample by reactive magnetron sputtering. The 2-inch diameter with 99.995% high purity Tantalum (Ta) and Tungsten (W) (KJ.Lesker), Ar and O_2 were used as the sputtered target, sputtered gas, and reactive gas, respectively. During the film deposition The growth parameter of TaO and WO3 thin films are listed in Table 3.2 In addition, the thickness of the TaO and WO_3 layer was set at 10, 20, 30, 50, and 70 nm, which was controlled through the deposition rate and time.

TABLE 3 -2 The deposition condition of TaO and WO_3 thin films.

Deposition Parameters	TaO	WO_3
Substrate	Au NPs samples	Au NPs samples
Target	Ta (99.995%)	W (99.995%)
Based Pressure	5×10^{-6} mTorr	5×10^{-6} mTorr
Operating Pressure	5×10^{-3} mTorr	5×10^{-3} mTorr
Ar Flow rate	15 sccm	15 sccm
O_2 Flow rate	7 sccm	7 sccm
Sputtering power (DC-pulse)	150 Watt	150 Watt
Rotation Speed	20 rpm	20 rpm

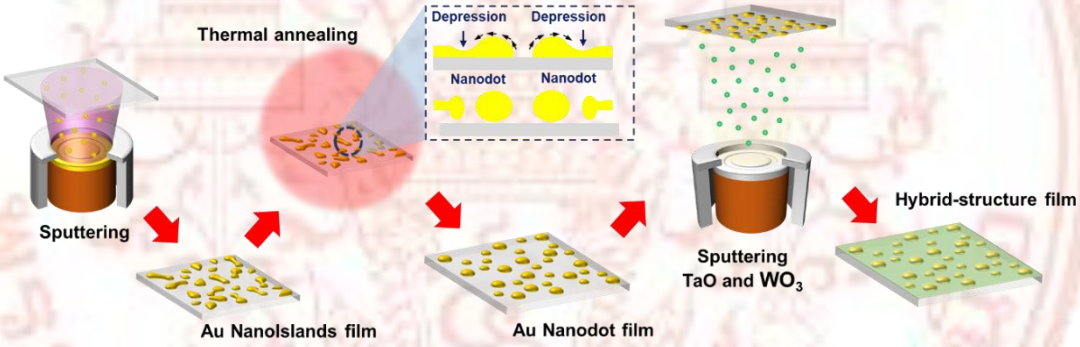

FIGURE 3 -4 Schematic diagram of LSPR-based VOCs optical sensors fabrication process

3.4 The Structure Analyses of TaO and WO_3 the Ultra-Thin Films

3.4.1 Field Emission Scanning Electron Microscopy (FE-SEM)

Scanning electron microscope of Hitachi, model SU8030, installed at NSTDA Characterization and Testing Service Center; NCTC) is used to analyze the thickness and physical structure of thin films in perspective. Cross section view and surface analysis of thin films in top view of tantalum oxide thin film. The working principle is that electrons are produced. From the origin of the field-emission source is accelerated by an electric field and determined direction with a set of magnetic lenses, resulting in a beam of electrons that travels across the surface of the sample to create Secondary electrons are detected and interpreted as

an image signal. To reveal the characteristics of thin film samples in specific positions, magnification was in the range of 50,000 and 100,000.

FIGURE 3 -5 The field-emission scanning electron microscope (FE-SEM; SU8030) used to analyze the morphology of thin film

3.4.2 High-resolution Transmission Electron Microscope (HR-TEM)

The high-resolution transmission electron microscope (HRTEM; JEOL JEM-2010), as illustrated in Figure 3-6 (a), was used to determine microstructure of thin film especially for microcrystalline sample. The essence of HRTEM is to detect the electrons that are transmitted through the sample as an image. which shows clearly different microstructure phases of the specimen. Because the electron must be transmitted through the sample, the etching process is needed to reduce the thickness of sample to be less than a micron. In this research, the samples were etched by the focused ion beam (FIB; FEI Versa 3D dual beam) in FE-SEM unit as represented in Figure 3-6 (b).

(a) **(b)**

FIGURE 3 -6 (a) High-resolution transmission electron microscope (TEM, JEOL JEM-2010) and (right) field-emission electron microscope/focused ion beam (FE-SEM/FIB, FEI Versa 3D dual beam).

3.5 Optical Measurement

3.5.1 UV-VIS-NIR Spectrophotometer

The UV-VIS-NIR Spectrophotometer (Agilent Cary7000 with UMA) with universal reflectance accessory is used to determine transmission and reflection percentage within the spectral range of 400-800 nm at 1 nm intervals, located Photonic Technology Laboratory, NECTEC, as seen in Figure 3-7

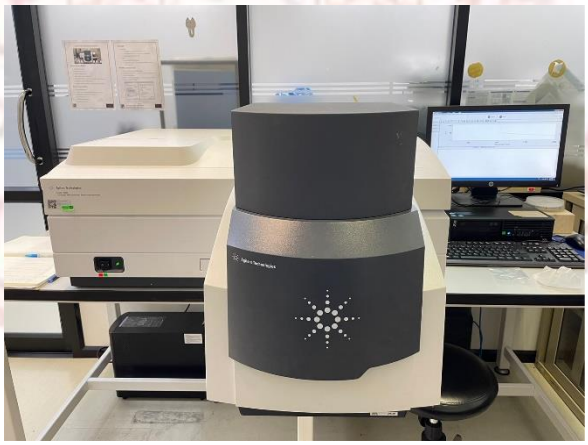

FIGURE 3 -7 UV/VIS spectrophotometer with the universal transmittance accessory, manufactured by Agilent technologies; Cary 7000 universal measurement spectrophotometer located at NECTEC, Thailand.

3.6 VOCs Optical Measurement Setup

The basic of optical gas sensors detection was based on the changing Refractive Index of the metal oxide material which depended on the chemical adsorption of the gas molecules. The metal oxide material detected the various VOCs. Generally, the gas sensor system had been investigated as shown in Figure 3-8. The VOCs sensitivity of sensors was tested with the vapor generating system using a gas bubbling technique. Air zero, containing 21% oxygen with dried and high-purity nitrogen, was used as a carrier gas, which adjusted its flow rate through the mass flow controller (MFC; MKS). In this system, MFC1 was used to control the gas flow rate of the main carrier gas while MFC2 was used for bubbling out the VOC vapor from the liquid source, including Formaldehyde (CH_2O), Isopropanol (C_3H_8O), Acetone (CH_3COCH_3), Methanol (CH_3OH) and Toluene ($C_6H_5CH_3$). The gases from both lines were directly into the chamber. The real-time measurements of optical transmittance spectra were performed with the VOCs sensitivity testing. The tungsten-halogen light source (Ocean Optics; HL2000) coupled to a fiber guided the light to incident on the back side of the sensor. The incident light was collimated by the lens and fixed as linear polarized light by a linear polarizer. The transmitted light was collected through the fiber probe, which was connected to a compact charge-coupled device (CCD) spectrometer (Thorlabs: CCS200) for spectrum analysis using Thorlabs OSA software. The instruments of the gas sensor system located at National electronic and computer technology center (NECTEC).

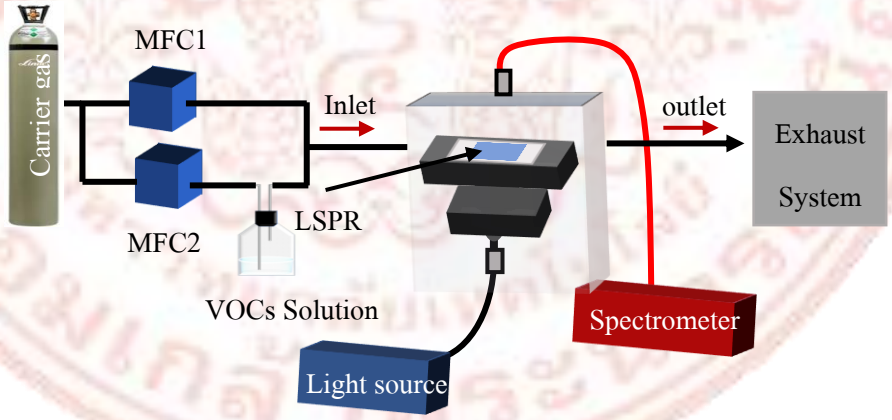

FIGURE 3 -8 Schematic diagram the vapor generating system for VOCs sensitivity testing of sensors

The gas sensor system was controlled by Gas testing Controller (beta) Lab-View control program from the computer as followed:

(a) Mass flow controller
(b) Connecting controller
(c) Concentration controller
(d) Total flowrate
(e) Startup time
(f) Gas inject time
(g) Gas stop time
(h) Status on testing time
(i) Concentration sequences
(j) Start/stop gas testing

FIGURE 3 -9 Gas testing Controller (beta) Lab-View control program

CHAPTER 4
RESULTS AND DISCUSSION

This chapter covers the results of the fabrication of Hybrid Au nanoplasmonics (Au NPs) with Tantalum oxide (TaO) and Tungsten oxide (WO_3) nanostructures, including their characteristics and their application for volatile organic compounds (VOCs) gas sensing applications.

The results of the experiments were arranged in three parts. Firstly, the main point was the preparation of Au NPs by DC-magnetron sputtering and combined with the solid-state dewetting technique in Section 4.1. In addition, the prepared samples were characterized by a Field-emission scanning electron microscope (FE-SEM).

Secondly, hybrid Au nanoplasmonics with Tantalum Oxide thin films were fabricated via a DC-magnetron sputtering system. The effect of deposition parameters on the film's morphologies and optical transmission were characterized by a Transmission electron microscope (TEM) and UV-VIS-NIR spectrophotometer. The proposed structure was used to simulate the electric field distributions via a COMSOL physics program through the finite element method (FEM) to analyze and discuss in Section 4.2. In addition, the hybrid Au NPs with TaO were used to test for sensitivity performance of the VOCs at room temperature and various VOC concentrations and kinds of gases, i.e., formaldehyde (CH_2O), isopropanol (C_3H_8O), acetone ($(CH_3)_2CO$), methanol (CH_3OH), and toluene ($C_6H_5CH_3$).

Thirdly, hybrid Au nanoplasmonics with Tungsten Trioxide thin films were fabricated via a DC-magnetron sputtering system. The effect of deposition parameters on the film's optical transmission were characterized by UV-VIS-NIR spectrophotometer in Section 4.3. In addition, the hybrid Au NPs with WO_3 were used to test for sensitivity performance of the VOCs at room temperature and various VOC concentrations and kinds of gases, i.e., formaldehyde (CH_2O), isopropanol (C_3H_8O), acetone ($(CH_3)_2CO$), methanol (CH_3OH), and toluene ($C_6H_5CH_3$).

4.1 Preparation of Au NPs film for by dc macnetron sputtering and thermal dewetting technique

4.1.1 The Thermal dewetting Effect of Au NPS nanostructure

The sputtered Au samples were annealed at 500°C for 2 hours in ambient air and cooled naturally to room temperature (25°C) by High-Temperature Furnace (EF-6L). The prepared Au sample was first observed in its surface morphologies via a field-emission scanning electron microscope (FE-SEM) to confirm the growth of Au nanodots on a glass substrate and determine their diameter and gap between them as shown in FIGURE 4-1

The surface of as-deposited Au and annealed Au films were compared before and after thermal dewetting through FE-SEM, as represented in FIGURE 4-1(a) and (b), respectively. The result shows that the as-sputtered Au film shows the nanoisland structure, which follows the Volmer-Weber model in the initial growth stage. After annealing, the nanoisland structure was changed to nanodots due to the solid-state dewetting effect. FIGURE 4.1(c) shows the solid-state dewetting process. When the nanoisland Au film was heated close to its melting point, depression occurred at the defect area on the film. Moreover, the boundary of the gold was shrunk, which made the Au particles disperse from the others and become nanodots after cooling back to the solid state.

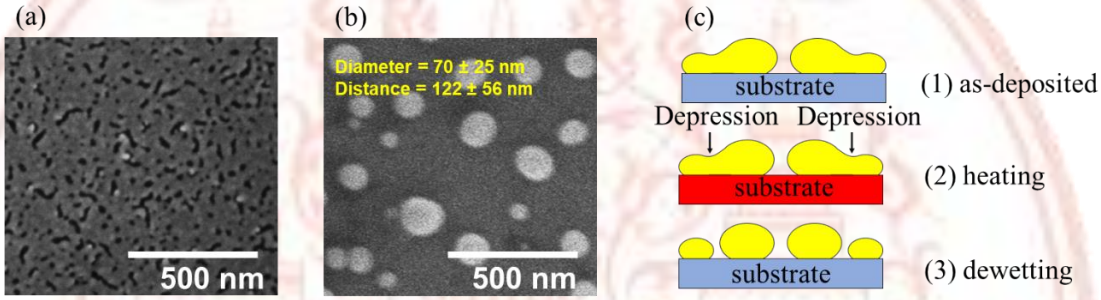

FIGURE 4 -1 FE-SEM images of (a) as-deposited and (b) annealed Au thin film, which transformed follows (c) solid-state dewetting effect.

The hybrid Au nanoplasmonic coated with TaO and WO_3 thin films were deposited by a DC magnetron sputtering system (AJA International, Inc., ATC 2000-F). The 2-inch-diameter tantalum (Ta) and tungsten (W) with 99.995% purity (KJ Lesker) were used as sputtering targets, while the Au NPs sample was used as substrates. High-purity argon (99.999%) and oxygen (99.999%) were used as sputtering and reactive gases, respectively. The base pressure of the deposition chamber was pumped down to 5.0×10^{-6} mbar using a mechanical pump and a turbomolecular pump. Prior to deposition, the Ta-target and W-target were pre-sputtered at 150 watts. During the deposition, the argon and oxygen flow rates were controlled at 15 and 7 sccm, respectively, which makes the operating pressure 5.0×10^{-3} mbar. The samples of thin films were divided into two sets:

1st set: The deposited films were labeled as Au NPs, Au-TaO 10nm, Au-TaO 20nm, Au-TaO 30nm, Au-TaO 50nm and Au-TaO 70nm for deposition thickness at 10, 20, 30, 50 and 70 nm with 826, 1652, 2478, 4130 and 5782 sec of coating time respectively.

2nd set: The deposited films were labeled as Au NPs, Au-WO_3 10nm, Au-WO_3 20nm, Au-WO_3 30nm, Au-WO_3 50nm and Au-WO_3 70nm for deposition

thickness at 10, 20, 30, 50 and 70 nm with 826, 1652, 2478, 4130 and 5782 sec of coating time respectively.

4.2 Preparation of Hybrid Au nanoplasmonics (Au NPs) and Tantalum oxide (TaO) film for the Volatile organic compound sensing application

4.2.1 The Deposition thickness effect

The effects of the parameters on morphologies and optical transmission of thin films were characterized by transmission electron microscopy (TEM) and UV-VIS-NIR spectrophotometers. FIGURE 4-2(a) shows the transmittance spectra of the Au NPs films and TaO film coated Au NPs at different TaO thicknesses. The result indicates that upon depositing ultra-thin TaO films, the resonance wavelength (the position at the lowest transmittance) was shifted due to the change in refractive index. A consistent red shift with a broadening resonance wavelength could be observed by increasing the thickness of ultra-thin TaO films Figure 4.2(b), which could be related to the shift in electric field density. Additionally, Figure 4.3 presents cross-sectional TEM images of the Au-TaO 50 nm sample. This confirmed that our fabrication method effectively controls the Au NPs on a glass slide substrate with full ultra-thin TaO film layer coverage.

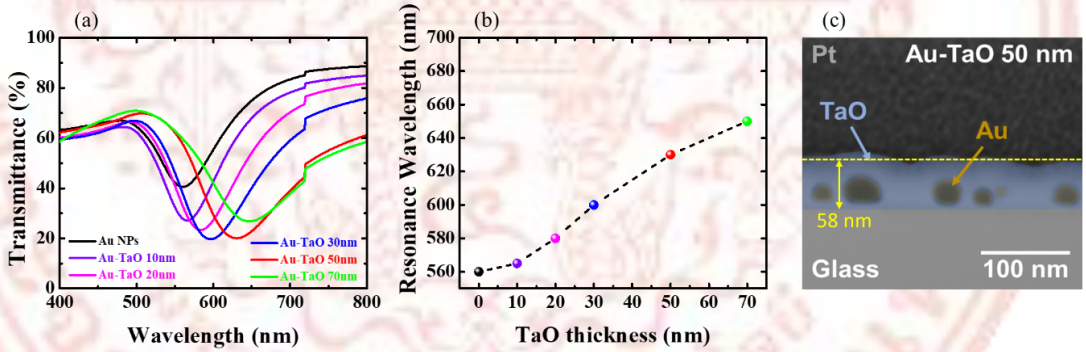

FIGURE 4 -2 (a) Optical transmittance spectra with (b) determined LSPR resonance wavelength of fabricated LSPR-based VOCs optical sensors and (c) cross-sectional TEM image of Au-TaO50nm sample.

4.2.2 Simulation the electric field distribution of Au NPs and hybrid Au NPs and Tantalum Oxide (TaO)

To investigate the effect of the thin TaO film, the electric field distribution was evaluated numerically using the two-dimensional finite element method in COMSOL Multiphysics software. The model was created for one unit cell of Au nanoplasmonics coated with a thin TaO film on a glass slide substrate, with Floquet boundary conditions to account for periodicity. The model includes a 100 nm-thick glass layer, circular Au nanoparticles with a 17 nm radius, a thin TaO film layer, and 300 nm of air, as illustrated in FIGURE 4-3 Different thicknesses of the thin TaO film coated on the Au nanoparticles were compared. The input for each periodic port in the model was set with the x-component electric field amplitude vector, and the angle of incidence was set at 0 degrees in the z-direction. The refractive index of the glass slide (quartz) is 1.5. The average electric field in the x-component (Ex) above the Au-TaO area (monitor) is computed and compared in FIGURE 4-3. The results show different induced electric field distributions related to the TaO thickness. The average Ex on the top surface of Au NPs, Au-TaO10nm, Au-TaO20nm, Au-TaO30nm, Au-TaO50nm, and Au-TaO70nm were determined as 1.12×105 V/m, 1.46×105 V/m, 1.39×105 V/m, 1.41×105 V/m, 1.49×105 V/m, and 1.46×105 V/m, respectively. Based on the bulk refractive index sensing, the LSPR resonance peak shifts provide information about the surface of the plasmonic nanoparticles. This characteristic enables localized sensing for highly enhanced E-field intensity; as a result, the local refractive index changes from the molecular detection near the surface.

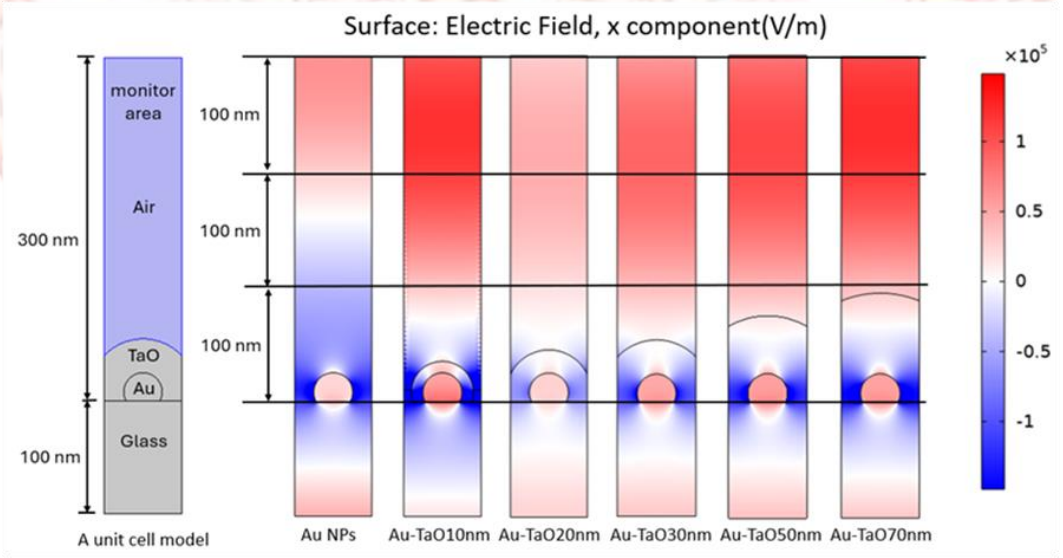

FIGURE 4 -3 Electric field distribution simulations of Au NPs and TaO-coated Au NPs at different film thicknesses.

4.2.3 Sensitivity for Volatile organic compound of Hybrid Au nanoplasmonics and Tantalum Oxide

The prepared samples were tested firstly for the sensitivity of acetone $(CH_3)_2CO$), isopropanol (C_3H_8O), methanol (CH_3OH), toluene ($C_6H_5CH_3$) and formaldehyde (CH_2O) at a concentration of 40% by the vapor generating system. The shift of resonance wavelength was determined when the VOC molecules were bubbled and fed into the gas testing chamber for 10 minutes, as represented in FIGURE 4-4. The results clearly showed the different sensitivity related to the thickness of the TaO layer.

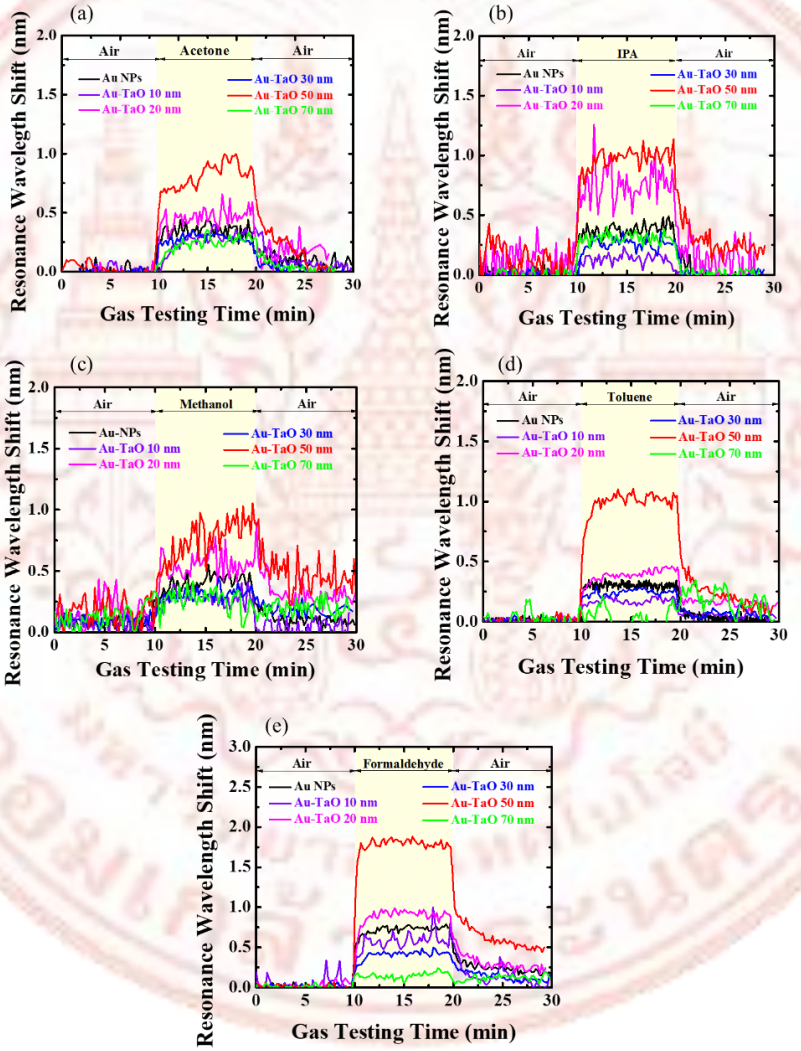

FIGURE 4 -4 Resonance wavelength shift signals from fabricated sensors testing with 40% concentration of (a) acetone (b) isopropanol (c) methanol (d) toluene and (e) formaldehyde respectively.

The Au-TaO50nm sample showed the highest resonance wavelength shift, which was better than the bare Au NPs. Moreover, greater sensitivity from the Au-TaO50nm sample agrees with previous electric field simulation results in section 4.2.2.

In addition, The Au-TaO50nm sample showed the best resonance wavelength shift of 1.80 nm, which was better than the bare Au NPs sensor by 2.5 times due to the TaO layer trapping the formaldehyde molecules better than the Au NPs through the chemical bonding on its surface.

Due to the result of resonance wavelength shift, The Au-TaO 50nm shows the best performance of sensitivity with Formaldehyde. The Au NPs and Au-TaO50nm sensors were tested with the multi-loop of formaldehyde at varied concentrations from 25% to 40% with 5% intervals as compared in FIGURE 4-5 The results showed the improved resonance wavelength shift related to increased formaldehyde concentrations for both sensors. The Au-TaO50nm represented the greater resonance wavelength shift at all testing concentrations compared to the bare Au NPs sensor. Notably, formaldehyde was detected at a small level, diluted at a concentration of 25%.

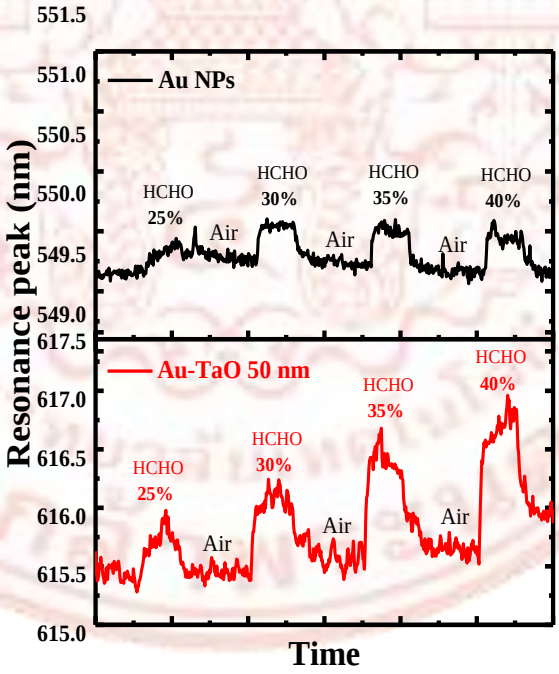

FIGURE 4 -5 Resonance wavelength tracking along multi-loop of formaldehyde sensitivity testing at varied concentrations from 25% to 40%.

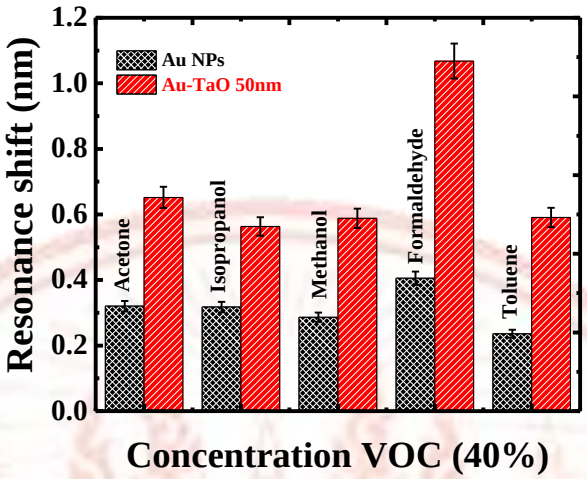

FIGURE 4 -6 Comparison of resonance shift along different VOC sensitivity testing at a concentration of 40% using Au NPs and Au-TaO50nm sensors.

The selectivity of both bare Au NPs and Au-TaO50nm sensors was tested using 5 types of VOCs at a concentration of 40%, as shown in FIGURE 4-6. The result indicated that Au-TaO50nm showed greater sensitivity to all VOC types compared to the bare Au NPs. This observation aligns with the simulated electric field result described in section 4.2.2. Furthermore, the Au-TaO50nm demonstrated high selectivity towards the formaldehyde, possibly due to the chemical reaction and bonding between the TaO surface and formaldehyde.

4.3 Preparation of WO_3 Hybrid nanoparticle structure film for the Volatile organic compound sensing application

4.3.1 The Deposition thickness effect

The effects of the parameters on optical transmission of thin films were characterized by UV-VIS-NIR spectrophotometers. FIGURE 4-7 (a) shows the transmittance spectra of the Au NPs films and WO_3 film coated Au NPs at different WO_3 thicknesses. The result indicates that upon depositing ultra-thin WO_3 films, the resonance wavelength (the position at the lowest transmittance) was shifted due to the change in refractive index. A consistent red shift with a broadening resonance wavelength could be observed by increasing the thickness of ultra-thin WO_3 films FIGURE 4-7 (b)

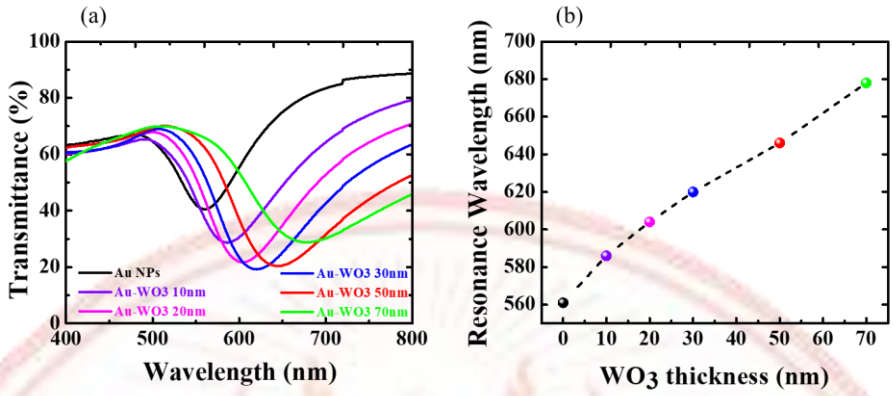

FIGURE 4 -7 (a) Optical transmittance spectra with (b) determined LSPR resonance wavelength of fabricated LSPR-based VOCs optical sensors

4.3.2 Sensitivity for Volatile organic compound of Hybrid Au nanoplasmonics and Tungsten Trioxide

In the same VOC sensing setup sequence as hybrid Au nanoplasmonics and tantalum oxide is section 4.2.3. The prepared samples were tested firstly for the sensitivity of acetone $(CH_3)_2CO$), methanol (CH_3OH), isopropanol (C_3H_8O), formaldehyde (CH_2O) and toluene ($C_6H_5CH_3$) at a concentration of 40% by the vapor generating system. The shift of resonance wavelength was determined when the VOC molecules were bubbled and fed into the gas testing chamber for 10 minutes, as represented in FIGURE 4-8. The results clearly showed the different sensitivity related to the thickness of the WO_3 layer.

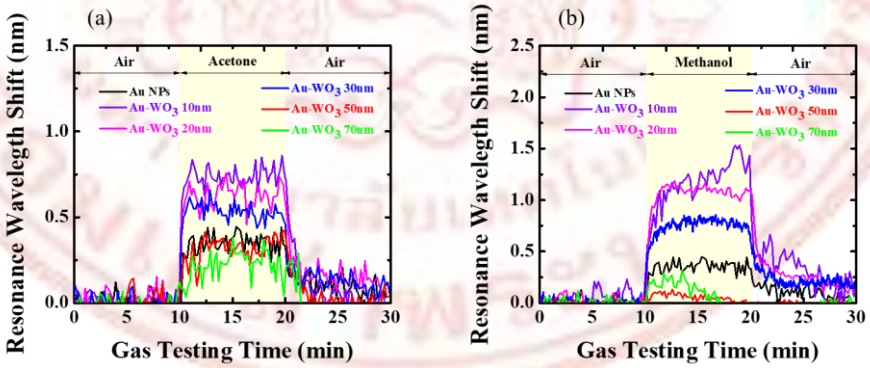

FIGURE 4 -8 Resonance wavelength shift signals from fabricated sensors testing with 40% concentration of (a) acetone (b) methanol (c) isopropanol (d) formaldehyde and (e) Toluene respectively.

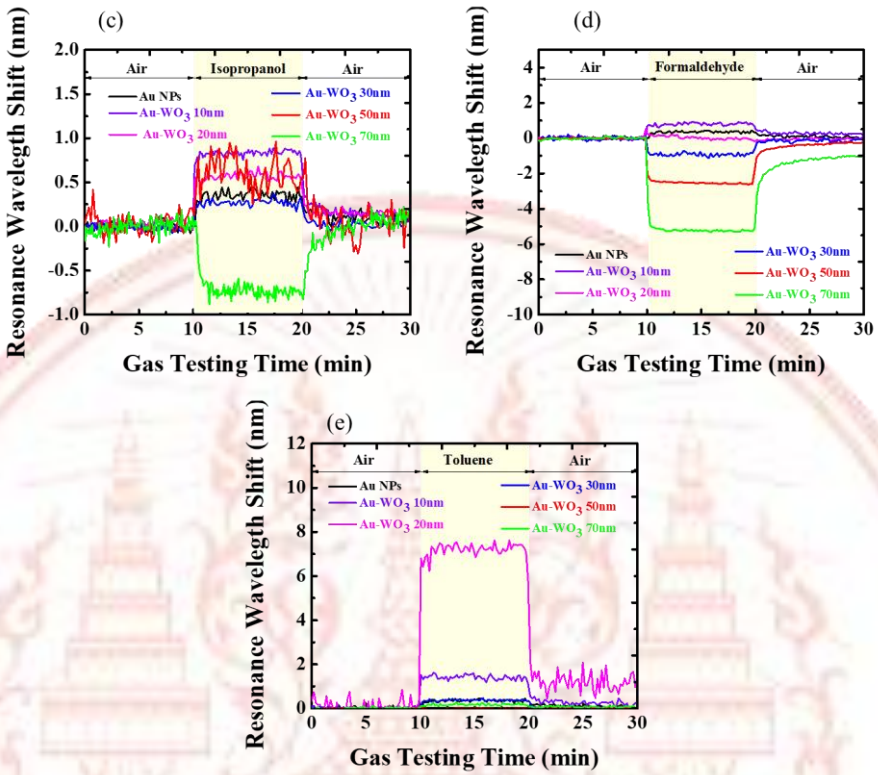

FIGURE 4 -8 (CONTINUED) Resonance wavelength shift signals from fabricated sensors testing with 40% concentration of (a) acetone (b) methanol (c) isopropanol (d) formaldehyde and (e) Toluene respectively.

The result in this section shows The Au-WO_3 10nm sample showed the highest resonance wavelength shift, which was better than the bare Au NPs. Except for the Toluene sensing that shows The Au-WO3 20 nm have the highest sensitivity However, In this section some of sensing performance has a specific result like Isopropanol and Formaldehyde that show a minus sensitivity, Possibly WO_3 can undergo reactions that lead to degradation, particularly when used as a sensitive layer in environments with reactive chemicals or under specific environmental conditions (e.g., humidity, light exposure)[50].

Due to the result of Resonance wavelength shift, The Au-WO_3 20nm shows the best performance of sensitivity with Toluene. The Au NPs and The Au-WO_3 20nm sensors were tested with the multi-loop of Toluene at varied concentrations from 25% to 40% with 5% intervals as compared in FIGURE 4-9 .

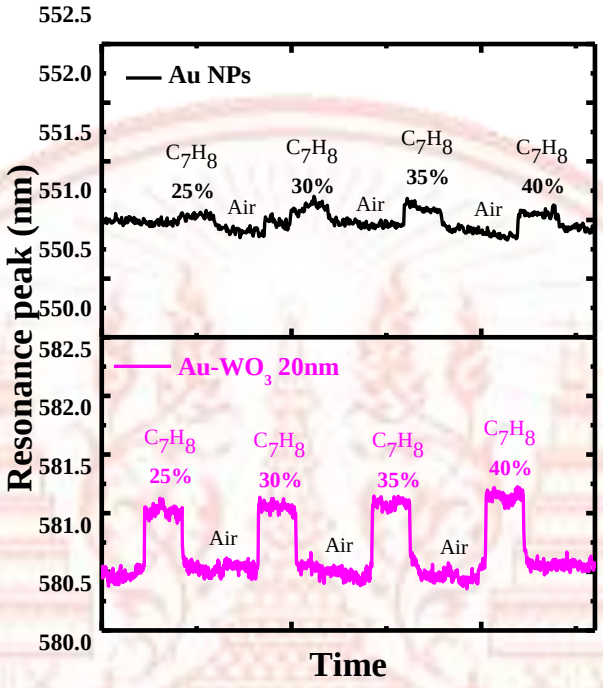

FIGURE 4 -9 Resonance wavelength tracking along multi-loop of toluene sensitivity testing at varied concentrations from 25% to 40%.

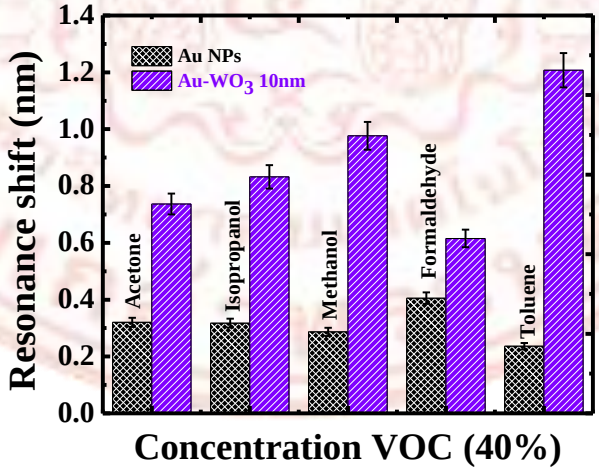

FIGURE 4 -10 Comparison of resonance shift along different VOC sensitivity testing at a concentration of 40% using Au NPs and Au-WO_3 20nm sensors.

The selectivity of both bare Au NPs and Au-WO_3 10nm sensors was tested using 5 types of VOCs at a concentration of 40%, as shown in FIGURE 4-10. The result indicated that Au-WO_3 10nm showed greater sensitivity to all VOC types compared to the bare Au NPs. Furthermore, the Au-WO_3 10nm demonstrated high selectivity towards the Toluene, possibly due to the chemical reaction and bonding between the WO_3 surface and Toluene.

CHAPTER 5
CONCLUSION

In this research, the aim was to fabricate of hybrid Au nanoplasmonics (Au NPs) with tantalum oxide (TaO) and tungsten oxide (WO_3) nanostructures by DC-magnetron sputtering which control film formation and structure, including their characteristics and their sensing performance for volatile organic compounds (VOCs) were also present.

5.1 Summary of the preparation of hybrid Au nanoplasmonics (Au NPs) with tantalum oxide (TaO)

In the first section, the fabrication of the Au NPs with a TaO thin film was based on DC-magnetron sputtering with Thermal dewetting technique. The morphologies of Au NPs was observed by field-emission scanning electron microscope (FE-SEM). The result shows the transmittance spectra of the Au NPs films and ultra-thin TaO film-coated Au NPs at different TaO thicknesses. The result indicates that upon depositing ultra-thin TaO films, the resonance wavelength was shifted due to the change in refractive index

The morphologies of TaO thin film nanostructures were controlled by various deposition time and various deposition thickness. At the deposition thickness of TaO 50nm the Au-TaO 50nm thin film on glass slide substrate was observed by a transmission electron microscope (TEM) a cross-sectional TEM images of the Au-TaO 50 nm sample confirmed that our fabrication method effectively controls the Au NPs on a glass slide substrate with full ultra-thin TaO film layer coverage.

The simulated electric field distributions indicated a correlation between the electric field density and the optimized TaO film thickness layer. The results show different induced electric field distributions related to the TaO thickness. The average Ex on the top surface of Au NPs, Au-TaO10nm, Au-TaO20nm, Au-TaO30nm, Au-TaO50nm, and Au-TaO70nm were determined as 1.12×105 V/m, 1.46×105 V/m, 1.39×105 V/m, 1.41×105 V/m, 1.49×105 V/m, and 1.46×105 V/m, respectively.

The prepared samples were tested firstly for the sensitivity of VOCs with the formaldehyde, isopropanol, acetone, methanol and toluene. at a concentration of 40% by the vapor generating system. The results clearly showed the different sensitivity related to the thickness of the TaO layer.

The sensitivity of Au-TaO50nm with a formaldehyde sample showed the highest resonance wavelength shift of 1.80 nm, which was better than the bare Au NPs sensor by 2.5 times due to the TaO layer trapping the formaldehyde molecules better than the Au NPs through the chemical bonding on its surface.

The Au NPs and Au-TaO50nm sensors were tested with the multi-loop of formaldehyde at varied concentrations from 25% to 40% with 5% intervals as compared. The results showed the improved resonance wavelength shift related to increased formaldehyde concentrations for both sensors. The Au-TaO50nm represented the greater resonance wavelength shift at all testing concentrations compared to the bare Au NPs sensor. However, the Au-TaO50nm had a longer recovery time, as indicated by the returned resonance wavelength shifting after the stopped feeding loop. It might be affected by the strong formaldehyde trapping of the TaO layer, which could reduce the recovery time by small heating to the sensors

5.2 Summary of the preparation of hybrid Au nanoplasmonics (Au NPs) with tungsten oxide (WO_3)

In the second section, the fabrication of the Au NPs with a WO_3 thin film was based on DC-magnetron sputtering with Thermal dewetting technique. The morphologies of WO_3 thin film nanostructures were controlled by various deposition time and various deposition thickness. At the deposition thickness.

The prepared samples were tested firstly for the sensitivity of VOCs with formaldehyde, isopropanol, acetone, methanol and toluene. at a concentration of 40% by the vapor generating system. The results clearly showed the different sensitivity related to the thickness of the WO_3 layer. However, some samples showed negative sensitivity responses to isopropanol and formaldehyde, possibly due to the WO_3 layer's porous, thin-film structure.

The sensitivity of Au-WO_3 20nm with a Toluene sample showed the highest resonance wavelength shift. The Au NPs and Au-WO_3 20nm sensors were tested with the multi-loop of Toluene at varied concentrations from 25% to 40% with 5% intervals as compared. The Au-WO_3 20nm represented the greater resonance wavelength shift at all testing concentrations compared to the bare Au NPs sensor.

However, The results showed the improved resonance wavelength shift not related to increased Toluene concentrations for both sensors. Possibly have some problems with the surface sensor after testing with other gas

Furthermore, the results from this section suggest that exploring various WO_3 morphologies for sensing VOC vapors at 40% concentration reveals significant differences among the samples. Overall, the Au-WO_3 10 nm sample demonstrated the highest sensitivity for detecting most VOCs, except for toluene, where the Au-WO_3 20 nm sample exhibited the highest sensitivity. This may be due to the density packing in the WO_3 layer resulting from the thin-film operating pressure deposition experiment.

Suggestion for further study

1. **Optimization of layer thickness and morphology**
   Further research on optimizing the thickness and morphology of TaO and WO_3 layers could enhance sensitivity and selectivity toward specific VOCs. Studying how different deposition methods impact layer structure and density would help improve sensor performance.
2. **Multi-layer and hybrid nanostructures**
   Investigating hybrid structures combining TaO and WO_3 with other plasmonic metals e.g. silver or creating multi-layered configurations could provide improved sensitivity, broader detection ranges, and enhanced stability.
3. **Long-Term stability and reusability testing**
   Conducting long-term stability studies to assess sensor degradation over time, as well as testing the reusability.
4. **Investigation parameters of sensitive layer**
   The results obtained for the fabricated gas sensing layers indicate unavoidable variations in film parameters when tested with different VOCs, Further research is needed to clarify the key factors such as gas interaction mechanisms, film thickness, and humidity that most significantly impact the performance of these sensing layers.
5. **Computational modeling and simulation studies**
   Using simulation tools to model for selectivity of VOC molecules.
6. **Broadening detection range and lowering limit of detection**
   expanding the detection range to include additional VOCs and lowering the limit of detection for existing VOC targets, making the sensors suitable for detecting trace amounts of harmful gases.

REFERENCES

[1] by Peder Wolkoff and A. Arbejdsmiljøinstituttet, “Volatile Organic Compounds Sources, Measurements, Emissions, and the Impact on Indoor Air Quality,” 1995.

[2] J.-L. Mai, W.-W. Yang, Y. Zeng, Y.-F. Guan, and S.-J. Chen, “Volatile organic compounds (VOCs) in residential indoor air during interior finish period: Sources, variations, and health risks,” *Hygiene and Environmental Health Advances*, vol. 9, p. 100087, Mar. 2024, doi: 10.1016/j.heha.2023.100087.

[3] R. Atkinson, “Atmospheric chemistry of VOCs and NOx,” *Atmos Environ*, vol. 34, no. 12–14, pp. 2063–2101, 2000, doi: 10.1016/S1352-2310(99)00460-4.

[4] F.W. Karasek and R.E. Clement, *Basic Gas Chromatography-Mass Spectrometry: Principles and Techniques*. 1988. Accessed: Nov. 09, 2024. [Online]. Available: https://books.google.co.th/books?hl=th&lr=&id=_WVDqDII63cC&oi=fnd&pg=PP1&dq=Karasek,+F.+W.,+%26+Clement,+R.+E.+(2012).+Basic+gas+chromatography-mass+spectrometry:+principles+and+techniques.+Elsevier.&ots=7kwIflO-mV&sig=ZDGgavvGQt6VPxuQ10iWpIvGnTs&redir_esc=y#v=onepage&q=Karasek%2C%20F.%20W.%2C%20%26%20Clement%2C%20R.%20E.%20(2012).%20Basic%20gas%20chromatography-mass%20spectrometry%3A%20principles%20and%20techniques.%20Elsevier.&f=false

[5] A. Kännaste, L. Copolovici, and Ü. Niinemets, “Gas Chromatography–Mass Spectrometry Method for Determination of Biogenic Volatile Organic Compounds Emitted by Plants,” 2014, pp. 161–169. doi: 10.1007/978-1-4939-0606-2_11.

[6] K.-H. Kim, S. A. Jahan, and E. Kabir, “A review of breath analysis for diagnosis of human health,” *TrAC Trends in Analytical Chemistry*, vol. 33, pp. 1–8, Mar. 2012, doi: 10.1016/j.trac.2011.09.013.

[7] A. D. Wilson and M. Baietto, “Applications and Advances in Electronic-Nose Technologies,” *Sensors*, vol. 9, no. 7, pp. 5099–5148, Jun. 2009, doi: 10.3390/s90705099.

[8] B. Szulczyński and J. Gębicki, “Currently Commercially Available Chemical Sensors Employed for Detection of Volatile Organic Compounds in Outdoor and Indoor Air,” *Environments*, vol. 4, no. 1, p. 21, Mar. 2017, doi: 10.3390/environments4010021.

[9] Y.-F. Sun *et al.*, “Metal Oxide Nanostructures and Their Gas Sensing Properties: A Review,” *Sensors*, vol. 12, no. 3, pp. 2610–2631, Feb. 2012, doi: 10.3390/s120302610.

[10] A. Mirzaei, S. G. Leonardi, and G. Neri, “Detection of hazardous volatile organic compounds (VOCs) by metal oxide nanostructures-based gas sensors: A review,” *Ceram Int*, vol. 42, no. 14, pp. 15119–15141, Nov. 2016, doi: 10.1016/j.ceramint.2016.06.145.

[11] B. T. Raut, P. R. Godse, S. G. Pawar, M. A. Chougule, D. K. Bandgar, and V. B. Patil, “Novel method for fabrication of polyaniline–CdS sensor for H2S gas detection,” *Measurement*, vol. 45, no. 1, pp. 94–100, Jan. 2012, doi: 10.1016/j.measurement.2011.09.015.

[12] E. Mahmoudi, “Electronic Nose Technology and its Applications,” *Sensors & Transducers Journal*, vol. 107, pp. 17–25, 2009, [Online]. Available: http://www.sensorsportal.com

[13] N. Srisuai *et al.*, “A Nanocolumnar Tantalum Oxide-Guided Mode Resonance Sensor for Volatile Organic Compounds,” *ACS Appl Nano Mater*, vol. 4, no. 9, pp. 9665–9672, Sep. 2021, doi: 10.1021/acsanm.1c02054.

[14] X. Zhang, Y. Gu, B. Huang, and C. Weng, “Advanced polymer grating fabrications: Surface-engineered structural colors for organic vapor sensing,” *J Colloid Interface Sci*, vol. 662, pp. 583–595, May 2024, doi: 10.1016/j.jcis.2024.02.025.

[15] I. Tanyeli *et al.*, “Nanoplasmonic NO_2 Sensor with a Sub-10 Parts per Billion Limit of Detection in Urban Air,” *ACS Sens*, vol. 7, no. 4, pp. 1008–1018, Apr. 2022, doi: 10.1021/acssensors.1c02463.

[16] Y. Xiong, J. Zhou, Z. Xing, and K. Du, “Cancer risk assessment for exposure to hazardous volatile organic compounds in Calgary, Canada,” *Chemosphere*, vol. 272, p. 129650, Jun. 2021, doi: 10.1016/j.chemosphere.2021.129650.

[17] M. Kutz, Ed., *Handbook of Environmental Engineering*. Wiley, 2018. doi: 10.1002/9781119304418.

[18] S. Rawat, “Food Spoilage: Microorganisms and their prevention,” *Pelagia Research Library Asian Journal of Plant Science and Research*, vol. 5, no. 4, pp. 47–56, 2015, [Online]. Available: www.pelagiaresearchlibrary.com

[19] N. W. Desrosier and J. N. Desrosier, *The technology of food preservation.*, no. Ed. 4. Westport, Connecticut: AVI Publishing Company, Inc., 1977.

[20] L. Gram, L. Ravn, M. Rasch, J. B. Bruhn, A. B. Christensen, and M. Givskov, “Food spoilage—interactions between food spoilage bacteria,” *Int J Food Microbiol*, vol. 78, no. 1–2, pp. 79–97, Sep. 2002, doi: 10.1016/S0168-1605(02)00233-7.

[21] J. Zhou *et al.*, “Surface plasmon resonance (SPR) biosensors for food allergen detection in food matrices,” *Biosens Bioelectron*, vol. 142, p. 111449, Oct. 2019, doi: 10.1016/j.bios.2019.111449.

[22] S. Kasani, K. Curtin, and N. Wu, “A review of 2D and 3D plasmonic nanostructure array patterns: fabrication, light management and sensing applications,” *Nanophotonics*, vol. 8, no. 12, pp. 2065–2089, Dec. 2019, doi: 10.1515/nanoph-2019-0158.

[23] W. A. Murray and W. L. Barnes, “Plasmonic Materials,” *Advanced Materials*, vol. 19, no. 22, pp. 3771–3782, Nov. 2007, doi: 10.1002/adma.200700678.

[24] Stefan Alexander Maier, *Plasmonics: Fundamentals and Applications*. 2007.

[25] E. Petryayeva and U. J. Krull, “Localized surface plasmon resonance: Nanostructures, bioassays and biosensing—A review,” *Anal Chim Acta*, vol. 706, no. 1, pp. 8–24, Nov. 2011, doi: 10.1016/j.aca.2011.08.020.

[26] S. Yue *et al.*, “Gold-implanted plasmonic quartz plate as a launch pad for laser-driven photoacoustic microfluidic pumps,” *Proceedings of the National Academy of Sciences*, vol. 116, no. 14, pp. 6580–6585, Apr. 2019, doi: 10.1073/pnas.1818911116.

[27] K. M. Mayer and J. H. Hafner, “Localized surface plasmon resonance sensors,” Jun. 08, 2011. doi: 10.1021/cr100313v.

[28] Horprathum M., “A Comparative Study of Reactive Magnetron Sputtering TiO2 Thin Films,” 2009.

[29] “FABRICATION AND STUDY OF ITO THIN FILMS PREPARED BY MAGNETRON SPUTTERING Dissertation zur Erlangung des Grades Content,” 2003.

[30] Milton Ohring, *Materials Science of Thin Films: Depositon and Structure*. 2002.

[31] K. Ellmer, “Magnetron sputtering of transparent conductive zinc oxide: relation between the sputtering parameters and the electronic

properties," *J Phys D Appl Phys*, vol. 33, no. 4, pp. R17–R32, Feb. 2000, doi: 10.1088/0022-3727/33/4/201.

[32] W. Y. Chiu, C. H. Wu, H. L. Kao, E. S. Jeng, J. S. Chen, and C. C. Jaing, "The optical properties and applications of AlN thin films prepared by a helicon sputtering system," *Journal of Vacuum Science & Technology A: Vacuum, Surfaces, and Films*, vol. 20, no. 3, pp. 843–847, May 2002, doi: 10.1116/1.1470512.

[33] JUNG WON CHO, "Pulsed DC reactive magnetron sputtering of aluminum nitride thin films.," 2002.

[34] J. A. Thornton, "Substrate heating in cylindrical magnetron sputtering sources," *Thin Solid Films*, vol. 54, no. 1, pp. 23–31, Oct. 1978, doi: 10.1016/0040-6090(78)90273-0.

[35] Kiyotaka Wasa, Isaka Kanno, and Hidetoshi Kotera, *Handbook of Sputter Deposition Technology*. 1992.

[36] P. Eiamchai, P. Chindaudom, A. Pokaipisit, and P. Limsuwan, "A spectroscopic ellipsometry study of TiO2 thin films prepared by ion-assisted electron-beam evaporation," *Current Applied Physics*, vol. 9, no. 3, pp. 707–712, May 2009, doi: 10.1016/j.cap.2008.06.011.

[37] Matthew M. Hawkeye, Michael T. Taschuk, and Michael J. Brett, *Glancing Angle Deposition of Thin Films: Engineering the Nanoscale*. 2014.

[38] J. M. Ngaruiya, "Fundamental processes in growth of reactive DC magnetron sputtered thin films," 2004.

[39] J. A. Thornton, "HIGH RATE THICK FILM GROWTH," 1977. [Online]. Available: www.annualreviews.org

[40] J. A. Thornton, "Influence of substrate temperature and deposition rate on structure of thick sputtered Cu coatings," *Journal of Vacuum*

Science and Technology, vol. 12, no. 4, pp. 830–835, Jul. 1975, doi: 10.1116/1.568682.

[41] R. Messier, A. P. Giri, and R. A. Roy, "Revised structure zone model for thin film physical structure," *Journal of Vacuum Science & Technology A: Vacuum, Surfaces, and Films*, vol. 2, no. 2, pp. 500–503, Apr. 1984, doi: 10.1116/1.572604.

[42] P. J. Kelly and R. D. Arnell, "Development of a novel structure zone model relating to the closed-field unbalanced magnetron sputtering system," *Journal of Vacuum Science & Technology A: Vacuum, Surfaces, and Films*, vol. 16, no. 5, pp. 2858–2869, Sep. 1998, doi: 10.1116/1.581432.

[43] P. B. Barna and M. Adamik, "Fundamental structure forming phenomena of polycrystalline films and the structure zone models," *Thin Solid Films*, vol. 317, no. 1–2, pp. 27–33, Apr. 1998, doi: 10.1016/S0040-6090(97)00503-8.

[44] A. Matthews, *Advanced Surface Coatings: a Handbook of Surface Engineering*. 2012.

[45] F. Ruffino and M. G. Grimaldi, "Controlled dewetting as fabrication and patterning strategy for metal nanostructures," *physica status solidi (a)*, vol. 212, no. 8, pp. 1662–1684, Aug. 2015, doi: 10.1002/pssa.201431755.

[46] M. Kang, S.-G. Park, and K.-H. Jeong, "Repeated Solid-state Dewetting of Thin Gold Films for Nanogap-rich Plasmonic Nanoislands," *Sci Rep*, vol. 5, no. 1, p. 14790, Oct. 2015, doi: 10.1038/srep14790.

[47] J. Liu *et al.*, "Fabrication of Au network by low-degree solid state dewetting: Continuous plasmon resonance over visible to infrared region," *Acta Mater*, vol. 188, pp. 599–608, Apr. 2020, doi: 10.1016/j.actamat.2020.02.050.

[48] S. W. Ong, B. L. Ong, and E. S. Tok, “Optical and chemical stability of sputtered-Au nanoparticles and film in ambient environment,” *Appl Surf Sci*, vol. 488, pp. 753–762, Sep. 2019, doi: 10.1016/j.apsusc.2019.05.233.

[49] J. Liu *et al.*, “Fabrication of Au network by low-degree solid state dewetting: Continuous plasmon resonance over visible to infrared region,” *Acta Mater*, vol. 188, pp. 599–608, Apr. 2020, doi: 10.1016/j.actamat.2020.02.050.

[50] B. Bouchikhi *et al.*, “Formaldehyde detection with chemical gas sensors based on WO3 nanowires decorated with metal nanoparticles under dark conditions and UV light irradiation,” *Sens Actuators B Chem*, vol. 320, p. 128331, Oct. 2020, doi: 10.1016/j.snb.2020.128331.

VITA

Name	Kiratikarn Changpradub
Thesis Title	Development of hybrid plasmonics and metal oxide nanostructure chips for VOCs optical sensing device
Major Field	Materials Engineering
Biography	Miss Kiratikarn Changpradub completed her Bachelor of Engineering from King Mongkut's University of Technology North Bangkok and Master of Engineering in Materials Engineering at the same institution. In 2022, she joined the Opto-Electrochemical Sensing Research Team (OEC) at the National Electronics and Computer Technology Center (NECTEC) as a research student, where she focused on plasmonic materials and optical sensors until 2024. Her research interests include nanofabrication, plasmonic sensors, and materials science. She has presented her findings on nanoplasmonic materials at the International Conference on Radiation and Emission in Materials and published a paper in the journal Physica Status Solidi (a), titled "Hybrid Nanoarchitectronics of Tantalum Oxide-Coated Gold Nanoparticles as Localized Surface Plasmon Resonance-Based Sensors for Volatile Organic Compounds Detection.